Cell

Resource

Multimodal imaging of gene expression, morphology, and activity of the same neuron

Graphical abstract

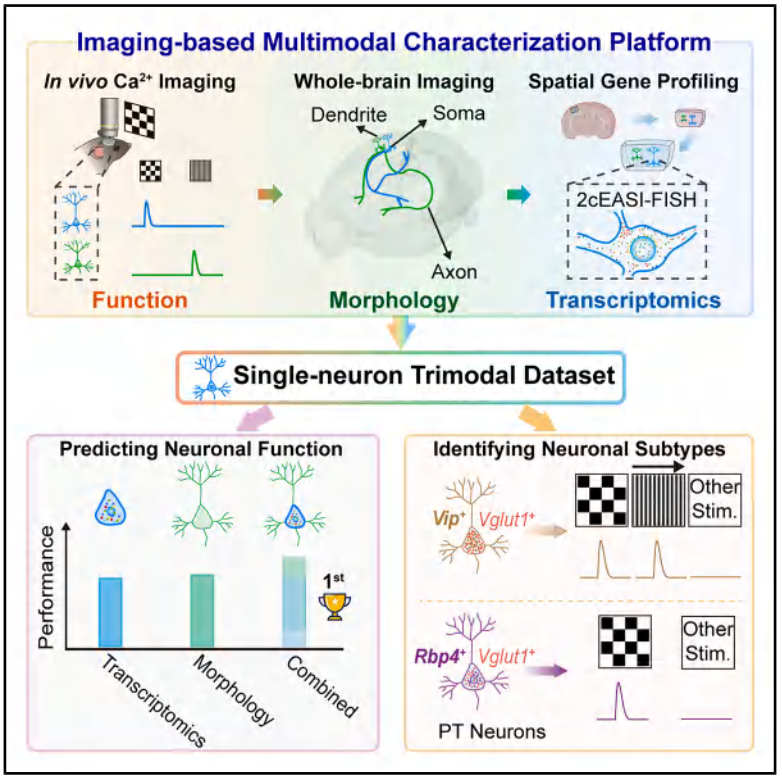

Highlights

- Imaging-based multimodal characterization platform enables trimodal neuronal profiling
- Subcellular RNA localization correlates with neuronal morphology and function
- Morphology and transcriptomics are complementary in predicting neuronal function
- *Vglut1*$^{+}$/*Vip*$^{+}$ pyramidal tract neurons in medial VISp define a distinct response subtype

Authors

Yuchen Zhao (赵钰琛), Ziqi Shi (石子琦), Xinglan Liu (刘星兰), ..., Ninglong Xu (徐宁龙), Shengjin Xu (徐圣进), Kai Wang (王凯)

Correspondence

sxu@ion.ac.cn (S.X.), wangkai@ion.ac.cn (K.W.)

In brief

This study establishes an imaging-based multimodal characterization (IMC) platform to link *in vivo* activity, whole-brain morphology, and spatial gene expression in the same cortical projection neurons. Applied to the mouse visual cortex, IMC reveals complementary morphological and molecular predictors of visual responses, identifies a neuronal subtype defined by trimodal profiling, and provides a ground-truth resource for multimodal integration.

Zhao et al., 2026, Cell *189*, 1–18
August 20, 2026
https://doi.org/10.1016/j.cell.2026.05.041

CellPress

Please cite this article in press as: Zhao et al., Multimodal imaging of gene expression, morphology, and activity of the same neuron, Cell (2026), https://doi.org/10.1016/j.cell.2026.05.041

Cell

CellPress

Resource

Multimodal imaging of gene expression, morphology, and activity of the same neuron

Yuchen Zhao (赵钰琛),[1,2,4] Ziqi Shi (石子琦),[1,2,4] Xinglan Liu (刘星兰),[1,2,4] Lin Cong (丛林),[1,4] Peng Yu (余鹏),[1,5] Xiaoxue Shi (史晓雪),[1] Lu Bai (白璐),[1] Yujie Zhang (张宇杰),[1,6] Liqin Gu (顾立钦),[1] Xiaofei Wang (王晓飞),[1] Chenxi Jin (金晨希),[1] Liuqin Qian (钱柳钦),[1] Wei Deng (邓伟),[1] Xinhe Zhang (张新贺),[1] Tielin Zhang (张铁林),[1,2] Ninglong Xu (徐宁龙),[1,2] Shengjin Xu (徐圣进),[1,2,7,*] and Kai Wang (王凯)[1,2,3,*]

[1]Institute of Neuroscience, State Key Laboratory of Brain Cognition and Brain-Inspired Intelligence Technology, Center for Excellence in Brain Science and Intelligence Technology, Chinese Academy of Sciences, Shanghai 200031, China

[2]University of Chinese Academy of Sciences, Beijing 100049, China

[3]School of Life Science and Technology, ShanghaiTech University, Shanghai 201210, China

[4]These authors contributed equally

[5]Present address: Leads Bio-Technology Co., Ltd., Shanghai 201101, China

[6]Present address: Max Planck Institute for Brain Research, Frankfurt 60438, Germany

[7]Lead contact

*Correspondence: sxu@ion.ac.cn (S.X.), wangkai@ion.ac.cn (K.W.)

https://doi.org/10.1016/j.cell.2026.05.041

SUMMARY

Elucidating the relationships among *in vivo* activity, brain-wide projection, and gene expression is critical for understanding neuronal functions, but characterizing these modalities for the same neuron remains technically challenging. Here, we developed a trimodal platform combining *in vivo* Ca^{2+} imaging, morphological reconstruction of single neurons in cleared whole brains, and post hoc imaging-based *in situ* transcriptomic profiling in thick brain sections. We applied this platform to the mouse primary visual cortex (VISp) and obtained trimodal profiles for 141 intratelencephalic (IT) and pyramidal tract (PT) neurons. We found that regional axonal arborization, soma location, transcriptomic signatures, and subcellular RNA localization emerged as informative predictors for distinguishing neurons preferentially responsive to different visual stimuli. Importantly, morphological and transcriptomic features are complementary and, when integrated, can better predict neuronal function. Thus, this trimodal platform enables a comprehensive understanding of the relationships among gene expression, morphological diversity, and functional properties of single neurons.

INTRODUCTION

The brain produces behavior through the collective activity of large numbers of neurons. Since the functional capacity of a neuron is shaped by its gene expression, morphology, and whole-brain connectivity, a central goal in neuroscience is to understand how these biological features collectively determine the functional role of each neuron.[1–3] Accordingly, trimodal integration of gene expression, whole-brain projections, and *in vivo* activity within the same neuron is essential for elucidating the fundamental molecule-structure-function relationships.[3] However, systematic trimodal analysis of the same neuron at the whole-brain level has remained difficult to implement in practice.

Recent technological advances have enabled separate high-throughput characterization of *in vivo* activity, morphology, and gene expression, yet multimodal integration still requires approaches that can bridge traditional barriers across different modalities. Current strategies for linking neuronal activities to molecular features include co-registration of *in vivo* Ca^{2+} activity with post hoc gene profiling of tissue sections.[4–9] Linking neuronal activity to complete morphology typically involves recording from sparsely labeled neurons followed by whole-brain reconstruction of neuronal processes.[10–12] Electron microscopic reconstruction after *in vivo* recording of neuronal activities can integrate neuronal function with local synaptic connectivity.[13–16] Relationships between neuronal morphologies and molecular features have traditionally been studied through morphological characterization of genetically targeted neurons,[1,17] and DNA barcoding methods now offer high-throughput simultaneous mapping of axon projections and transcriptomes with some compromise in morphological details.[18,19] For deeper multimodal profiling, RNA sequencing following patch-clamping (Patch-seq) captures local neuronal morphology, transcriptomes, and intrinsic electrophysiological properties, most commonly in isolated brain slices.[20–22] This information can be further linked to axon projections in separate

Please cite this article in press as: Zhao et al., Multimodal imaging of gene expression, morphology, and activity of the same neuron, Cell (2026), https://doi.org/10.1016/j.cell.2026.05.041

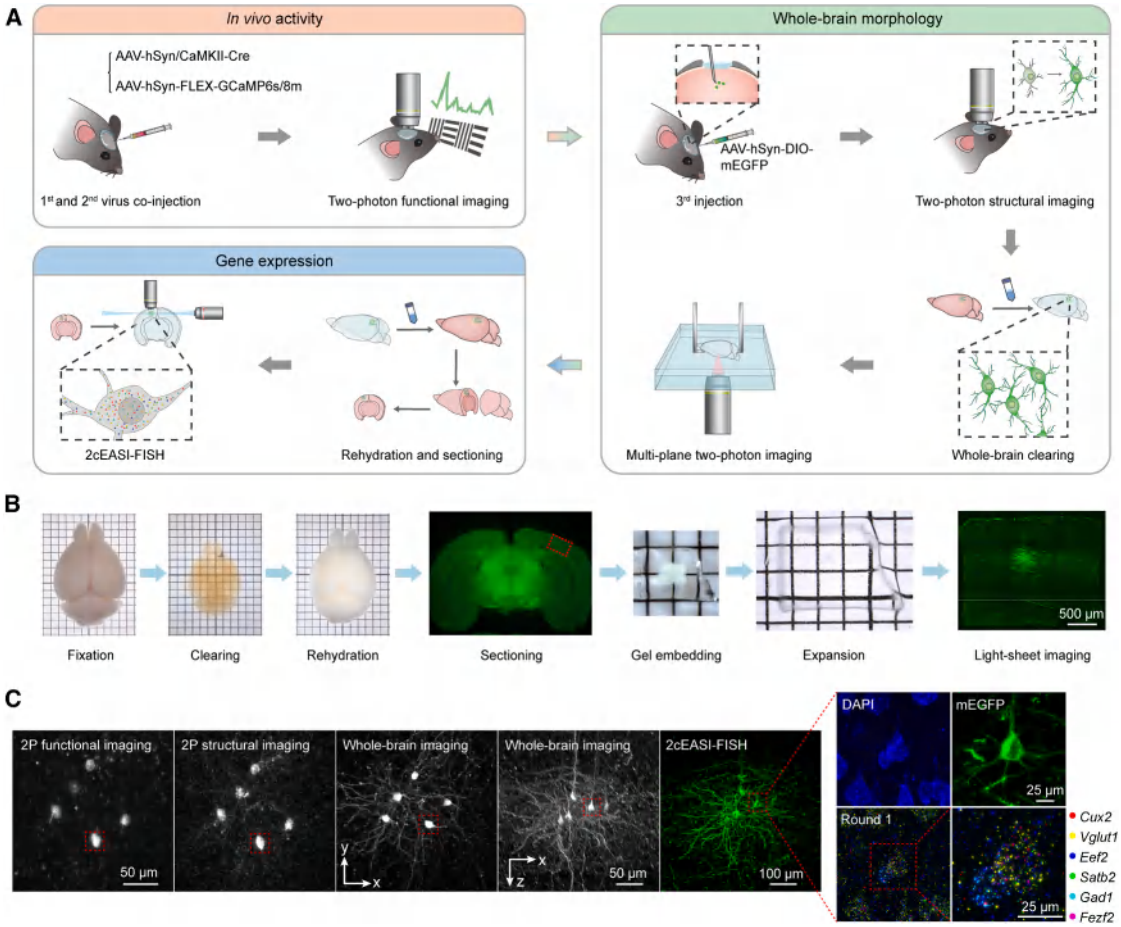

Figure 1. Overview of IMC platform for integrated functional, structural, and molecular profiling of single neurons

(A) Workflow of imaging-based multimodal characterization (IMC) pipeline.

(B) Representative images of the same brain at key processing stages, including fixation after functional imaging, whole-brain clearing for structural imaging, rehydration after structural imaging, brain sectioning, gel embedding, and expansion for light-sheet imaging of gene expression. Scale bar, 500 μm.

(C) Representative multimodal imaging of the same neurons across sequential stages. Right, enlarged view of a structurally reconstructed neuron showing molecular markers detected in round 1. Scale bars, 50 μm, 100 μm, and 25 μm as indicated in the corresponding panels.

single-neuron reconstruction datasets using local dendritic morphology.[23]

Despite these advances, integrating *in vivo* activity, complete morphology, and gene expression of the same neuron poses major methodological hurdles, primarily due to challenges in preserving structural/molecular integrity and tracking single-neuron identity across modalities. Optical imaging, with its high spatial resolution, can potentially address these challenges when combined with various molecular, structural, and activity monitoring methods. To overcome the compatibility issues, we developed an ''imaging-based multimodal characterization'' (IMC) platform that preserves mRNA molecules, fluorescent signals, and tissue integrity for high-resolution trimodal imaging. Using IMC, we obtained a trimodal dataset of 141 cortical projection neurons in the mouse primary visual cortex (VISp), including each neuron's specific visual response property, whole-brain projection pattern, and gene-expression profile with subcellular RNA localization. Thus, this IMC platform could support future studies aimed at elucidating the relationships among neuronal activity, morphology, and gene-expression patterns of single neurons.

RESULTS

Experimental platform for IMC

To characterize the relationships among neuronal activities, morphology/connectivity features, and gene-expression profiles of single neurons, we developed an IMC platform, in which data for the three modalities were sequentially obtained (Figure 1A). In step 1, we performed *in vivo* two-photon Ca^{2+} imaging in awake mice. Neuronal expression of Ca^{2+} indicators was achieved by co-injecting two viruses: one encoding Cre recombinase and the other encoding a Cre-dependent GCaMP6s/8m construct. The Cre-expressing virus was injected at low titer to achieve sparse and random labeling, enabling later complete morphological reconstruction of labeled neurons.[24,25] In this study, we focused

Please cite this article in press as: Zhao et al., Multimodal imaging of gene expression, morphology, and activity of the same neuron, Cell (2026), https://doi.org/10.1016/j.cell.2026.05.041

on the VISp and characterized neuronal responses to contrast-reversing checkerboard and drifting grating visual stimuli. After functional imaging, we injected a third virus encoding Cre-dependent membrane-targeted enhanced green fluorescent protein (mEGFP) to enhance structural labeling for high-quality morphological reconstruction. To verify mEGFP expression in the functionally imaged neurons, we performed *in vivo* two-photon structural imaging within the same field of view (FOV), generating a 3D reference template for cross-modality image registration.

In step 2, we performed whole-brain morphological imaging of single neurons. The brain was extracted and optically cleared using an optimized organic solvent-based clearing method balancing transparency, fluorescence preservation, and processing complexity (STAR Methods). Then, we developed a multi-plane two-photon microscope (MP-TPM) to image this intact cleared brain. In step 3, we performed molecular profiling of tissue sections from the cleared mouse brains. The cleared brain was rehydrated and coronally sectioned prior to gene-expression profiling (Figure 1B). To retain sufficient structural information for cross-modality registration, we performed 3D imaging of single mRNA molecules in thick brain sections using a dual-color hairpin-encoded variant of expansion-assisted iterative-fluorescence *in situ* hybridization (2cEASI-FISH), which doubles the per-round gene-detection throughput relative to the original EASI-FISH.[26] Because high-resolution spatial and morphological features were preserved across modalities, the IMC pipeline enables trimodal integration of data from the same neurons (Figure 1C; Video S1).

In vivo Ca^{2+} imaging of sparsely labeled mouse visual cortical neurons

To illustrate the workflow of the IMC platform, we conducted *in vivo* Ca^{2+} imaging on sparsely labeled VISp neurons in head-fixed mice. We optimized viral titer and injection volume (Table S1) to achieve sparse labeling of tens of neurons per mouse. We presented contrast-reversing checkerboard and drifting sinusoidal grating visual stimuli, which differ in contrast dynamics, orientation, and motion features, to facilitate the identification of function-morphology relationships (Figure 2A). We also recorded facial movements to examine the modulatory effects of behavioral states on visual cortical neurons. Using a generalized linear model (GLM), we identified neurons that showed significant responses to different types of visual stimuli or temporally associated with facial movements (Figures 2B and 2C; STAR Methods). In total, we recorded Ca^{2+} activity of 207 neurons (from 12 mice), among which 39 responded selectively to the checkerboard stimulus, 36 to the grating stimuli, and 19 neurons to both. Additionally, 22 neurons showed activity that correlated with facial movements. The remaining 91 neurons, which displayed regular spontaneous Ca^{2+} transients without significant correlation with either visual stimuli or facial movements, were categorized as non-responsive (Figures 2D and 2E; STAR Methods), although they may respond to other visual stimuli not tested here. The GLM employed a set of basis functions to adaptively capture the diverse Ca^{2+} dynamics observed across individual cells and between the two indicators (GCaMP6s and GCaMP8m). We found no significant differences in functional characterization between neurons expressing either indicator (Figures S1A–S1C).

Enhanced fluorescence labeling for structural imaging

To prepare for subsequent morphological imaging, we induced mEGFP expression through viral injection following *in vivo* two-photon imaging. The virus was delivered with an injection pipette that directly penetrated the flexible window implanted in the initial surgery (STAR Methods). Compared with previous methods using GCaMP for both functional and structural imaging,[11,12] mEGFP re-labeling offered two advantages: first, mEGFP labeled thin and distal neurites more efficiently than cytosolic GCaMP, and second, decoupling structural imaging from GCaMP expression avoided the need for excessive GCaMP expression that could impair neuronal responses and viability. Using this approach, mEGFP fluorescence was observed in 93.7% ± 8.3% of GCaMP-labeled neurons, and GCaMP fluorescence was observed in 85.2% ± 14.1% of mEGFP-labeled neurons (mean ± SD, n = 13 fields of view from 9 mice; Figures S1D and S1E). The occasional mismatches in co-labeling are likely attributable to the stochastic nature of viral infection and to false-negative identification of GCaMP labeling in neurons with low expression levels. We also optimized the GCaMP viral titer to minimize competition with mEGFP expression. Overall, mEGFP produced about 6-fold brighter neurite labeling than GCaMP (Figures S1F and S1G).

Development of multi-plane two-photon imaging for whole-brain axon tracing

Following structural labeling, brains were extracted for whole-brain imaging and single-neuron reconstruction. To preserve tissue and mRNA integrity critical for subsequent gene-expression profiling, we optimized an organic solvent-based brain clearing pipeline (Figures S2A and S2B; STAR Methods) and developed an MP-TPM comprising eight scanning beams for high-resolution imaging of single neurons in cleared whole brains (Figures 3A and S2C). Compared with existing techniques for large-scale single-neuron reconstruction,[27,28] MP-TPM imaging preserved the whole brain and allowed for later optimized brain sectioning that ensured the local integrity of labeled regions for molecular imaging. In contrast to light-sheet microscopy, MP-TPM offers two advantages: (1) greater tolerance for the imperfect transparency that frequently occurred in deep brain regions, and (2) enhanced resistance to refractive-index (RI) mismatches that could degrade excitation-detection co-alignment in light-sheet imaging.[29] Additionally, MP-TPM overcomes the slow imaging speed of conventional TPM by splitting the excitation laser into eight beams, acquiring images from eight channels simultaneously. Importantly, unlike traditional multi-beam two-photon microscopes that distribute beams across different lateral locations within a single plane,[30,31] MP-TPM focused eight beams at axially displaced planes, allowing optimal integration with continuous galvo mirror scanning in the x-direction and stage scanning in the y-direction. This approach maximized both the scanning speed and the imaging FOV and minimized image stitching (Figure S2D), facilitating imaging of large samples. To ensure independent fluorescence detection from different planes, we maintained sufficient lateral separations between axially displaced foci. This beam splitting and 3D focusing were achieved using a holographic beam splitter (Figures 3B and S2E). Fluorescent signals from each channel were collected

Please cite this article in press as: Zhao et al., Multimodal imaging of gene expression, morphology, and activity of the same neuron, Cell (2026), https://doi.org/10.1016/j.cell.2026.05.041

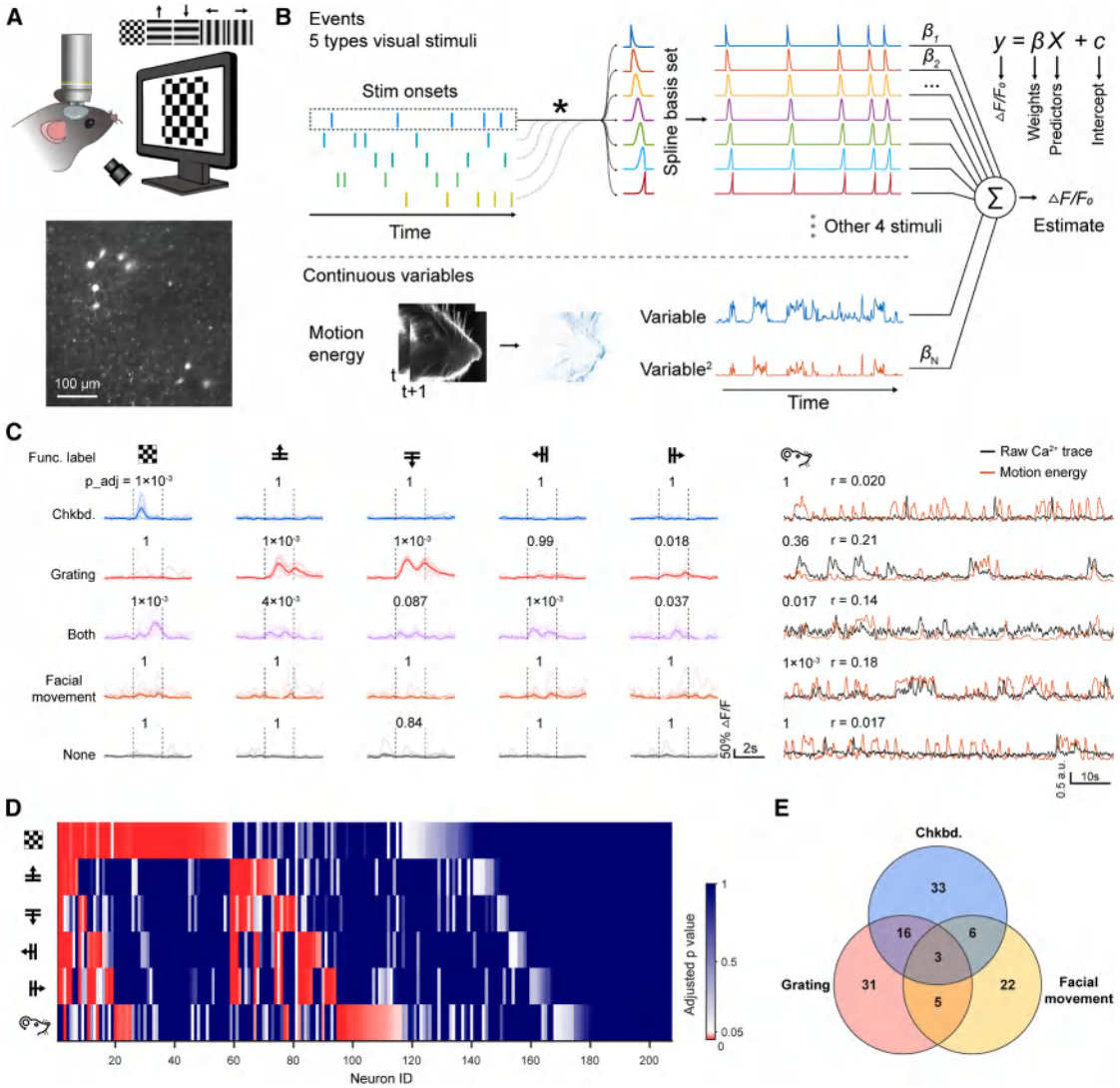

Figure 2. Imaging and characterization of *in vivo* activities of visual cortical neurons

(A) Simultaneous TPM Ca^{2+} imaging of sparsely labeled neurons (bottom) and facial movement monitoring during the visual stimuli presentation. Scale bar, 100 μm.

(B) GLM framework for characterizing Ca^{2+} responses to visual stimuli and facial movements. The model estimates $\Delta F/F_0$ as a linear combination of predictors, including visual responses fitted by convolving visual stimulus onsets with a spline basis, as well as continuous facial motion energy variables (linear and squared components) (STAR Methods).

(C) Functional responses of example neurons. Left: solid lines, mean response; light-colored lines, individual trial responses; trace scale bars, 50% $\Delta F/F_0$ and 2s. Dashed vertical lines, stimulus onset and offset. Right: raw Ca^{2+} activity (black) and motion energy component (orange); trace scale bars, 0.5 a.u. and 10 s. *p* values were derived from permutation-based F-tests comparing full and reduced models with Bonferroni correction. Pearson correlation coefficients (r) between Ca^{2+} activity and motion energy are indicated (STAR Methods).

(D) Statistical significance of functional responses of all imaged neurons in response to different types of visual stimuli and facial movement.

(E) Summary of the neuronal populations showing significant responses to presented visual stimuli and facial movement.

separately by large-core multimode fibers (Figure S2C). We used a customized objective (STAR Methods) that had an effective numerical aperture (NA) of 1.0 and a 6.5-mm working distance, with measured lateral and axial resolution of 0.5 and 2.5 μm (theoretical, 0.33 and 1.8 μm), respectively, within the 400-μm diameter FOV across all eight channels (Figures 3C and S2F). Each stage scan along the y-direction simultaneously captured eight images covering a volume of 400 × 10,000 × 16 μm^3. Approximately 6,000 stage scans covered the entire brain. To maximize imaging quality and accommodate the objective's limited working distance, the brain was flipped midway and imaged in two halves (Figure S2G).

In an example mouse brain, 48 neurons within an approximately 1-mm^2 VISp region were virally labeled (Figure 3D). The MP-TPM imaged the whole brain and enabled complete morphology reconstruction of 44 of them (Figure 3D; Video S2). Their primary axonal

Please cite this article in press as: Zhao et al., Multimodal imaging of gene expression, morphology, and activity of the same neuron, Cell (2026), https://doi.org/10.1016/j.cell.2026.05.041

CellPress

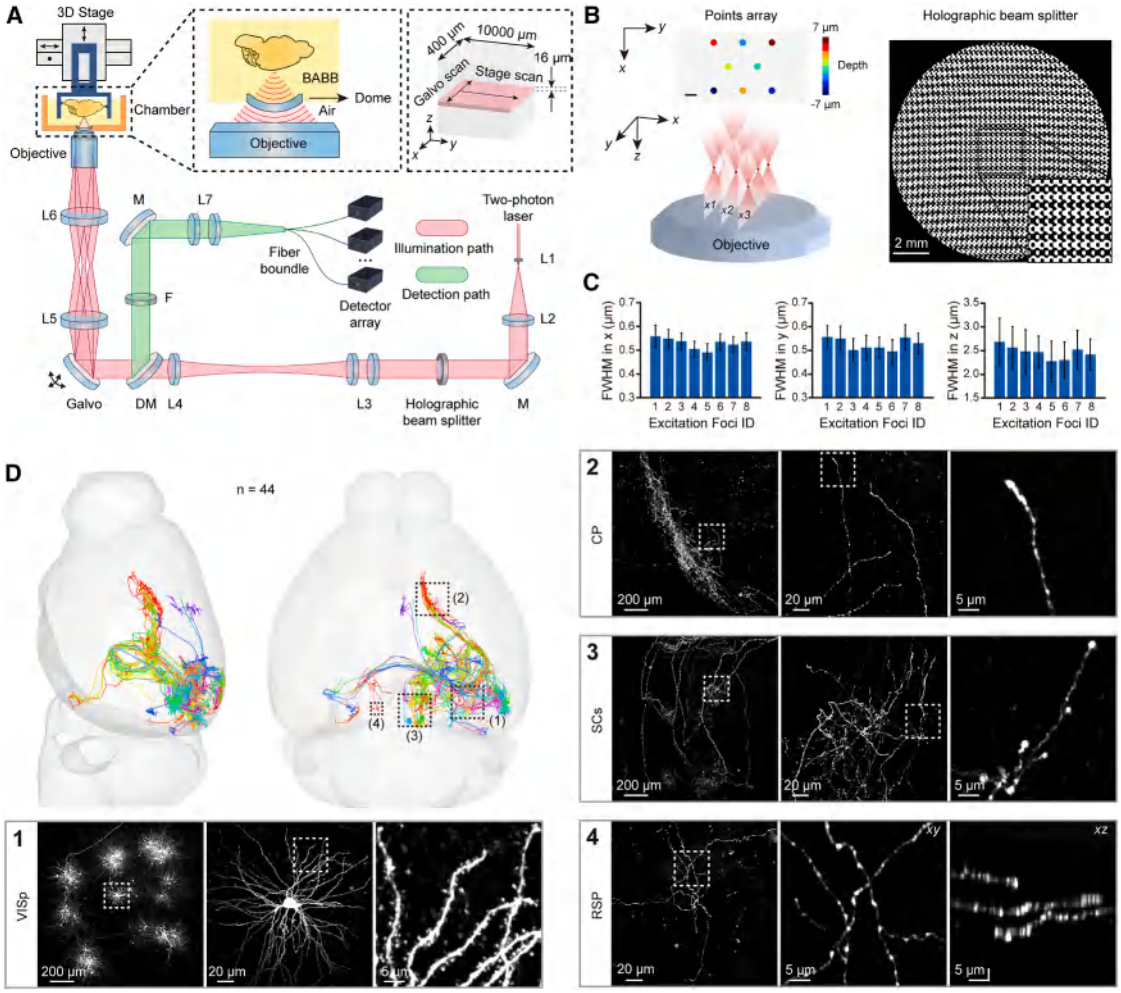

Figure 3. Robust whole-brain single-neuron morphology reconstruction using an MP-TPM

(A) Schematic of the MP-TPM. L1-L5, lenses; DM, dichroic mirror; F, emission filter; M, mirror. Insets: customized glass dome designed for imaging into a high-RI clearing medium using an air objective, and the coordinated scanning scheme using a galvo mirror and sample stage to achieve a large FOV.

(B) Parallelized excitation by eight focal spots. Left, spatial arrangement of eight focal spots; scale bar, 10 μm. Right, binary phase (0 and π) map of the holographic beam splitter; scale bar, 2 mm.

(C) Characterization of the resolutions achieved by the MP-TPM. Full width at half maximum (FWHM) of intensity profiles measured on 200-nm diameter fluorescence beads (n = 100). Data are presented as mean ± SD.

(D) Morphological reconstruction of 44 VISp neurons from a representative mouse brain and zoom-in views in the brain regions, including VISp, caudate putamen (CP), sensory-related superior colliculus (SCs), and contralateral retrosplenial area (RSP). Scale bars: 200 μm, 20 μm, and 5 μm as indicated in the zoomed views.

projection targets, including caudate putamen (CP), sensory-related superior colliculus (SCs), and contralateral retrosplenial area (RSP), were in line with the known targets of VISp neurons.[32,33] The total laser power measured after the objective was approximately 360 mW, corresponding to about 45 mW per focusing spot. We employed a long pixel integration time of 3.5 μs to ensure detection of weakly labeled structures. Typical photon counts per pixel were approximately 20 for autofluorescence and 800 for dendritic structures (Figure S2H). We observed small variations (σ = 7.5%) in signal intensity across channels, likely attributable to differences in detector gain, excitation, and collection efficiency. These variations were corrected offline before morphological reconstruction. Imaging one whole brain required ~100 h. The system reliably imaged more than 13 mouse brains with consistent performance throughout this study (Table S1). The preservation of the intact brain, combined with low-level photobleaching (Figure S2I), enabled multiple rounds of imaging on the same brain in case of interruption during imaging.

Morphological reconstruction of functionally characterized neurons

We performed whole-brain imaging on 12 mice and reconstructed 207 functionally characterized neurons, of which 170 and 132 met the quality criteria (STAR Methods) for axon and dendrite morphological reconstruction, respectively (Figures S3A and S3B). This represents an approximately 58% success rate for simultaneously obtaining *in vivo* activities and complete morphologies (Figures 4A, 4B, and S4). To make

Please cite this article in press as: Zhao et al., Multimodal imaging of gene expression, morphology, and activity of the same neuron, Cell (2026), https://doi.org/10.1016/j.cell.2026.05.041

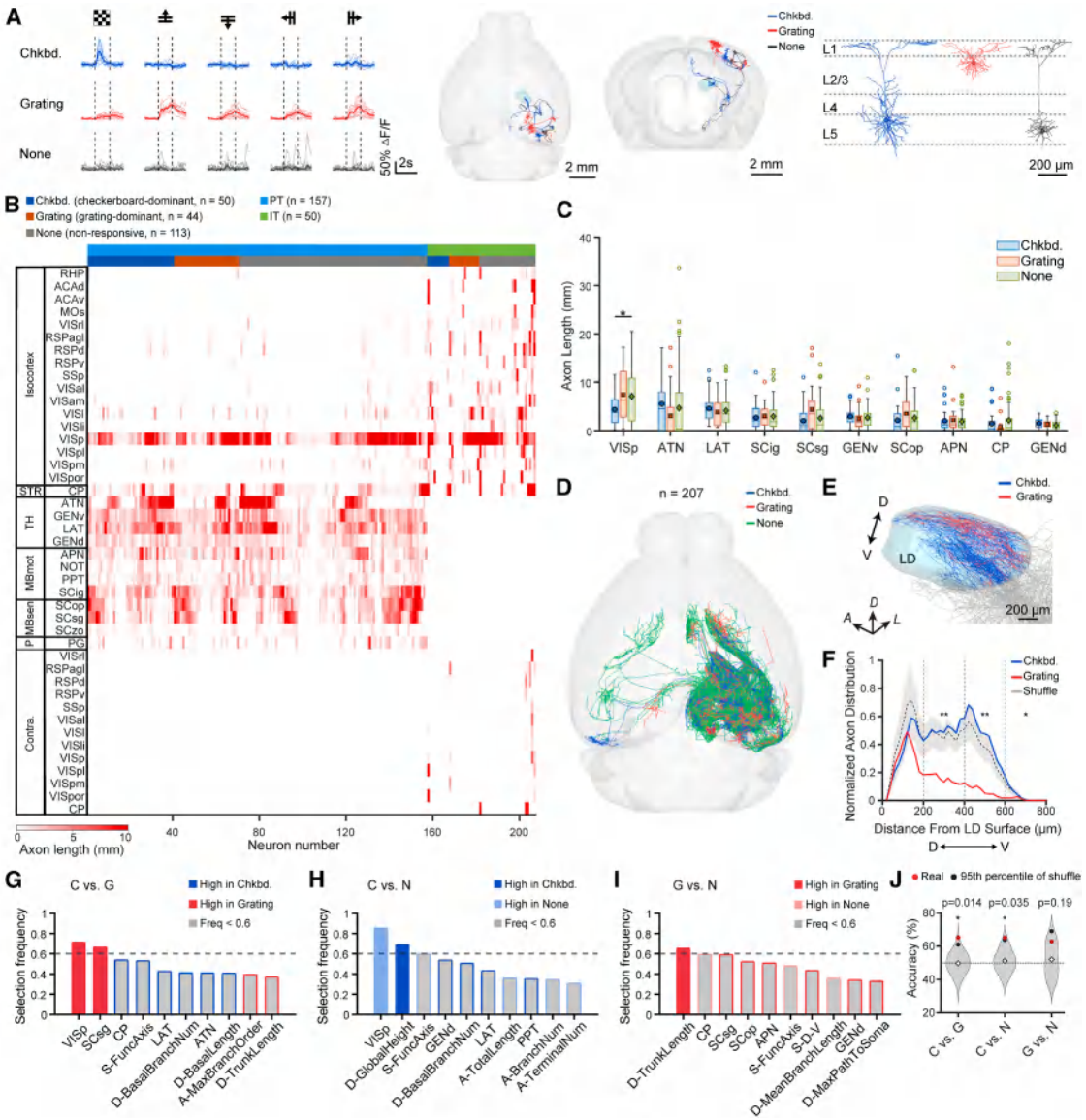

Figure 4. Linking neuronal function and the complete morphology of individual neurons

(A) *In vivo* activities, whole-brain projections, and local morphologies of three example neurons. Solid lines, mean response; light-colored lines, individual trial responses. Dashed vertical lines, stimulus onset and offset. Trace scale bars: 50% $\Delta F/F_0$ and 2s. Scale bars: 2 mm (whole-brain projection) and 200 μm (local morphology).

(B) Heatmap of axonal projection strengths across brain regions for all reconstructed neurons.

(C) Comparison of axonal projection strengths in major target regions across functionally distinct neuronal groups. Kruskal-Wallis test followed by Dunn's post hoc test with BH FDR correction (*$p < 0.05$).

(D) Complete morphologies of 207 functionally characterized neurons in the VISp.

(E) Distributions of axons from checkerboard- and grating-dominant neurons within (colored) and surrounding (gray) the laterodorsal thalamic nucleus (LD). Scale bar, 200 μm.

(F) Quantification of differential axon distributions along the dorsal-ventral (D-V) axis within the LD (STAR Methods). The black dashed line and shaded area represent the mean and 95% confidence interval of the shuffled distribution. The differences between grating-dominant neurons and the shuffled distribution are assessed using non-parametric permutation tests with Bonferroni correction (*$p < 0.05$; **$p < 0.01$).

(G–I) Feature selection based on LassoGLM analysis for pairwise predictions of functional identities using morphological features, including checkerboard-dominant vs. grating-dominant (G), checkerboard-dominant vs. non-responsive (H), and grating-dominant vs. non-responsive (I). The selection frequency threshold was set as 0.6. Features are color-coded based on the group in which they are elevated. Feature prefixes: A-, axonal morphology; D-, dendritic morphology; S-, soma location.

(J) Predictive accuracies of classification models based on real (red dots) and shuffled data (violin plots). Black dots, 95th percentile of shuffled. Dashed line, chance level (50% accuracy). C, checkerboard; G, grating; N, non-responsive. (*$p < 0.05$).

Statistics are provided in Table S3.

Please cite this article in press as: Zhao et al., Multimodal imaging of gene expression, morphology, and activity of the same neuron, Cell (2026), https://doi.org/10.1016/j.cell.2026.05.041

optimal use of available information, the number of neurons included in subsequent analyses varied depending on the specific data modalities required. No data were excluded without explicit justification. To facilitate analysis across animals, mouse brains were registered to the Allen CCFv3 atlas,[34] with registration errors below 20 μm (Figures S5A and S5B).

Based on the axon projection patterns of these 207 reconstructed neurons, we identified 157 pyramidal tract (PT) neurons and 50 intratelencephalic (IT) neurons.[24,35,36] Cortico-thalamic (CT) neurons were absent in our bimodal dataset, likely due to their deeper cortical location and the depth limitation of *in vivo* two-photon Ca^{2+} imaging. For 170/207 neurons that met the quality criteria for axon reconstruction, axonal endpoints were clearly identifiable (Figure S1H). We compared neurons that passed quality control for axonal reconstructions with previously published results.[11,24,36] The PT and IT neurons exhibited axonal lengths of 46.4 ± 13.1 mm (mean ± SD, n = 133) and 51.9 ± 41.0 mm (mean ± SD, n = 37), respectively, with no significant difference when compared with results from Peng et al.[36] (Figures S1I and S1J). While the visual cortical IT neurons reported in Winnubst et al.[24] showed greater axonal length, the small sample size (n = 7) and the inherent variability in IT neuronal morphologies[25] may account for observed differences. We also performed a similar analysis on neurons that passed quality control for dendritic reconstructions. The total dendritic lengths of PT and IT neurons were 8.9 ± 2.7 (mean ± SD, n = 99) and 6.3 ± 1.3 mm (mean ± SD, n = 33), respectively, in line with previous findings.[24,36]

It was shown that neurons in the mouse prefrontal cortex with distinct axon projection patterns exhibited preferential distribution patterns of their somata,[25] and the total length of the axonal arbors of a neuron positively correlated with that of its dendrites.[37] We thus examined whether these findings also apply to the mouse VISp. We categorized axon morphology into three subtypes: PT, ipsilateral projecting IT, and contralateral projecting IT. Contralateral projecting IT neurons were primarily located in the anterior region, while ipsilateral projecting IT neurons were mainly found in the center of the VISp (Figure S3C). The projection patterns of IT neurons exhibited considerable variability, consistent with previous reports.[25,36] By contrast, the projection patterns for PT neurons were more uniform. We then examined relationships between dendritic and axonal features of the same neuron and found significant correlations in many features (Figures S3D and S3E). For example, linear regression analysis on neurons with both high-quality reconstructions of axons and dendrites showed that the total length and branch number of dendritic arbors of PT neurons positively correlated with those of their axon arbors (total length, R^2 = 0.24, $p = 7.82 \times 10^{-7}$; branch number, R^2 = 0.23, $p = 2.02 \times 10^{-6}$; n = 91). Such correlation was not significant for IT neurons, presumably due to their highly variable morphology and the small sample size (n = 29).

Function-morphology correlation analysis of the same neuron

We next examined potential correlations between neuronal morphology and functional responses. With the current sample size, we found no significant correlation between each neuron's axon projection subtype and its visual response selectivity (Figure S3F). Visual response selectivity also did not vary significantly with somatic laminar depth (Figure S3G). We further performed pairwise classification using a GLM and confirmed that neither laminar position alone nor 3D positional information provided significant predictive power for distinguishing visual response subtypes (Figure S3H).

Next, we investigated whether detailed morphological features and axonal projection patterns correlated with the neuron's visual responses, focusing on PT neurons (n = 157). Within this group, 31 responded selectively to the checkerboard stimulus, 23 to drifting gratings, and 16 to both stimuli but typically with a bias toward one stimulus type. To simplify the analysis, we categorized visually responsive neurons into two groups: checkerboard-dominant (n = 40; 31 selective, 9 preferring) and grating-dominant (n = 30; 23 selective, 7 preferring) (Figure 4B; STAR Methods). The remaining 87 neurons were categorized as non-responsive.

We quantified axonal length in each brain region to generate projection patterns for all reconstructed neurons[25] (Figure 4B) and compared projection strengths, defined as the total axon length within a brain region (STAR Methods), of the three different functional groups across the 10 most strongly innervated brain regions (Figure 4C). Checkerboard-dominant neurons showed significantly weaker axonal projections within VISp than non-responsive neurons ($p$adj = 0.048, Kruskal-Wallis test followed by Dunn's post hoc test with Benjamini-Hochberg [BH] false discovery rate [FDR] correction). Full morphological reconstructions (Figures 4D–4F) revealed distinct laterodorsal thalamic nucleus (LD) projections: for grating-dominant neurons, the core and ventral LD innervations (STAR Methods) were significantly lower ($p < 0.0013$ and $p < 0.0013$, respectively; permutation test) than those of checkerboard-dominant neurons.

To systematically examine the correlation between morphology and visual response selectivity, we constructed a 38-feature vector including 22 morphology features, axonal projection strengths in 13 brain regions, and 3D soma location (Figures S5C and S5D; Table S2; STAR Methods). To better capture functionally relevant spatial organization, we mapped 3D soma location onto rotated axes fitted to the spatial distributions of functional subtypes (Figure S5E; STAR Methods). Using a Lasso-regularized GLM (LassoGLM), we ranked features by their selection frequency across 1,000 bootstrap iterations. To balance selection robustness and sensitivity, we retained the top features with selection probability exceeding 60% for further GLM analyses[38] and evaluated their predictive power (Figure S6A). Consistent with Figure 4C, the projection strength in VISp emerged as the strongest discriminator between checkerboard- and grating-dominant neurons, followed by projection strengths in SCsg (SC and superficial gray layer) (Figure 4G). For checkerboard-dominant vs. non-responsive neurons, both axonal projection pattern and dendritic morphology were identified as key predictors (Figure 4H). Pairwise GLM classifiers based on these selected features achieved accuracies significantly above chance for both comparisons (Figure 4J). By contrast, distinguishing grating-dominant from non-responsive neurons was more challenging. Only one feature passed the selection threshold (Figure 4I), and the resulting pairwise GLM classifier failed to achieve accuracy significantly above chance levels. Collectively, our results indicate that projection patterns

Please cite this article in press as: Zhao et al., Multimodal imaging of gene expression, morphology, and activity of the same neuron, Cell (2026), https://doi.org/10.1016/j.cell.2026.05.041

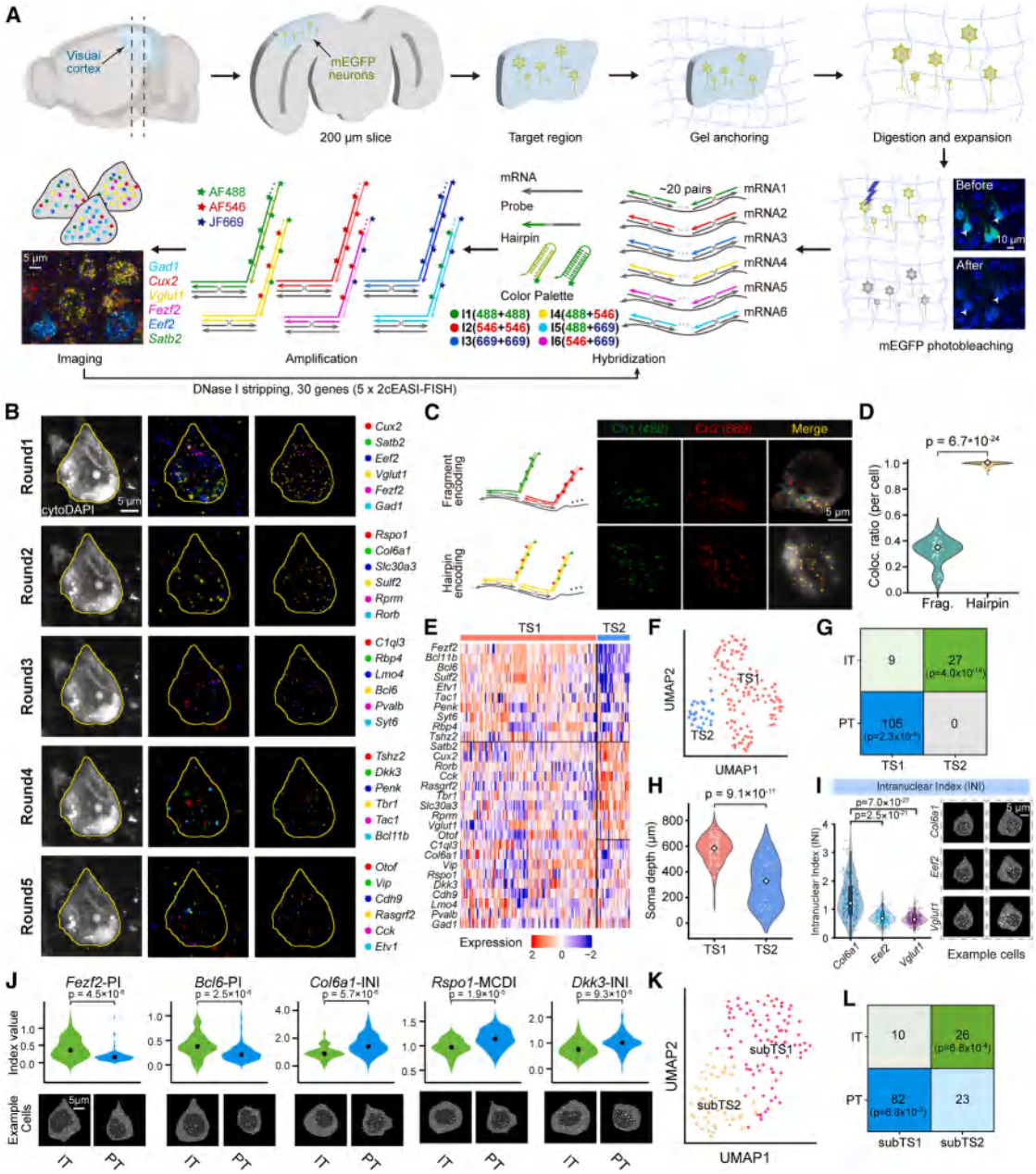

Figure 5. Concordance of transcriptomic and subRNA-Loc subtypes with projection types via trimodal 2cEASI-FISH

(A) Cross-modal 2cEASI-FISH workflow. Thick brain sections containing functionally and morphologically characterized neurons were processed by 2cEASI-FISH, enabling 3D registration of prior imaging with *in situ* gene-expression readouts. Dual-color HCR detects six genes per round; five rounds yield 30 genes. Scale bars: 10 μm and 5 μm, as indicated.

(B) Representative five-round 2cEASI-FISH readout. Left, cytoDAPI images with soma outlines; middle, raw 2cEASI-FISH images; right, decoded puncta for all 30 mRNA species. Scale bar, 5 μm.

(C) Fragment- vs. hairpin-encoding dual-color HCR-FISH. Left, encoding schemes; right, raw images showing *Vglut1* colocalization across 2 channels. Scale bar, 5 μm.

(D) Colocalization ratio per cell (STAR Methods) for fragment-encoding (n = 43, mean ± SD: 0.316 ± 0.095) vs. hairpin-encoding (n = 105, mean ± SD: 0.992 ± 0.015) (two-sided Wilcoxon rank-sum test, $p = 6.7 \times 10^{-24}$). White diamonds, medians; dots, cells.

(E) Heatmap of 29 marker-gene-expression levels across the transcriptomic subtypes (TS1 and TS2; STAR Methods). Genes are ordered by differential expression.

(F) Uniform manifold approximation and projection (UMAP) plot of transcriptomic profiles from (E), colored by transcriptomic subtype.

(G) Alignment of transcriptomic subtypes with projection types (IT vs. PT) shown as a contingency matrix (cell counts). Fisher's exact test.

(H) Laminar distribution of transcriptomic subtypes. Violin plots show soma depths; TS1 is enriched in L5, TS2 in L2/3. White diamonds, medians; dots, cells. Two-sided Wilcoxon rank-sum test.

(legend continued on next page)

Please cite this article in press as: Zhao et al., Multimodal imaging of gene expression, morphology, and activity of the same neuron, Cell (2026), https://doi.org/10.1016/j.cell.2026.05.041

and dendritic morphological features jointly specified functionally distinct VISp neurons.

In addition to morphological correlates of visual response selectivity, we further investigated differences between PT neurons selectively responding to visual stimuli vs. facial movements. LassoGLM analysis identified three features with > 60% selection probability, including global dendrite height and projection strengths in the posterior pretectal nucleus (PPT) and geniculate group, ventral thalamus (GENv) (Figure S3I). Although their combination did not yield significantly higher prediction accuracy in GLM-based classification, we observed significant differences in global dendrite height and GENv (Figures S3J and S3K). These features may serve as potential morphological markers, a possibility that warrants further investigation with larger datasets.

High-throughput 2cEASI-FISH for gene-expression profiling

To ensure efficient downstream gene-expression profiling while preserving the 3D structural integrity required for cross-modal registration, we rehydrated and coronally sectioned the brain after whole-brain morphological imaging. We then implemented an enhanced variant of EASI-FISH in thick brain sections. To increase throughput while avoiding spot-registration challenges across multiple imaging rounds in thick tissue,[39] we developed a dual-color hairpin-encoded EASI-FISH method (2cEASI-FISH) that exploits the inherent combinatorial logic of hairpin pairs in hybridization chain reaction (HCR) (Figure 5A). By engineering orthogonal hairpin sets and a custom mRNA-calling algorithm (Figures S7A and S7C; STAR Methods), we simultaneously detected six genes per round (Figure 5B). Compared with conventional dual-color fragment encoding, hairpin encoding achieved near-perfect dual-channel colocalization in thick tissue (Figures 5C and 5D; colocalization ratio: 0.316 ± 0.095 vs. 0.992 ± 0.015 (mean ± SD, n = 43 vs. 105 neurons); $p = 6.7 \times 10^{-24}$, two-sided Wilcoxon rank-sum test), ensuring accurate mRNA decoding.

We then performed five rounds of 2cEASI-FISH on all 207 neurons and obtained complete 30-gene-expression profiles for 141 of them, comprising 105 PT neurons and 36 IT neurons (Figure S3A) with high mRNA retention (Figure S7B). The target gene panel included 29 VISp neuron marker genes[32,40,41] and a reference housekeeping gene, *Eef2* (Figure 5B; STAR Methods). Although clearing and rehydration mildly reduced mRNA abundance, as reported previously,[42] expression patterns and molecular identities remained comparable to untreated controls (Figures S7D–S7F).

Concordance of transcriptomic subtypes with canonical projection types

Although genes enriched in projection types (IT vs. PT) have been reported, most evidence has relied on Cre drivers as gene-expression proxies[36,43] or on linking transcriptomes to target-defined projections via retrograde tracing[41,44] or barcode-based projection mapping.[45] A direct, same-cell alignment between gene-expression profiles and projection types defined by whole-brain morphology has remained limited. Using our trimodal same-neuron dataset, we asked whether transcriptomic subtypes align with canonical projection types. Unsupervised clustering based on 29 marker genes classified these excitatory neurons into two transcriptomic subtypes with distinct markers: TS1, *Fezf2*/*Bcl11b*/*Bcl6*; TS2, *Satb2*/*Cux2*/*Rorb* (Figures 5E and 5F; STAR Methods). Notably, a subset of excitatory neurons co-expressed *Vglut1* with traditionally inhibitory markers (*Vip*, *Gad1*, or *Pvalb*), a pattern also observed in the Allen Brain Cell Atlas (Figure S8A; STAR Methods).

These transcriptomic subtypes showed strong concordance with canonical projection types: 105/114 TS1 neurons matched PT neurons (vs. the PT fraction among all neurons, 105/141; $p = 2.3 \times 10^{-4}$, Fisher's exact test), whereas 27/27 TS2 neurons mapped to IT neurons (Figure 5G; vs. the IT fraction among all neurons, 36/141, $p = 4.0 \times 10^{-14}$, Fisher's exact test). This was consistent with enrichment of canonical IT markers (*Satb2* and *Cux2*) in TS2[46,47] (Figure 5E). Soma-depth analysis further showed that TS1 neurons were mainly in layer 5, whereas TS2 neurons were predominantly in layer 2/3 (Figure 5H; TS1 vs. TS2, $p = 9.1 \times 10^{-11}$; two-sided Wilcoxon rank-sum test), matching the laminar distributions of PT and IT neurons.[35]

We next examined whether transcriptomic differences underlie the greater morphological variability of IT neurons. Compared with PT neurons, IT neurons showed significantly greater pairwise divergence in axon length (Figure S8B; $p = 4.7 \times 10^{-49}$, two-sided Wilcoxon rank-sum test), higher heterogeneity in 29-gene-expression profiles (Figure S8C; $p = 1.6 \times 10^{-7}$) and greater variability of the IT marker *Rorb* (Figure S8E; $p = 2.4 \times 10^{-23}$). Within the IT population, however, overall 29-gene transcriptional distances did not correlate with axon-length divergence (Figure S8D; Spearman's r = −0.12, $p = 0.27$, Mantel test; STAR Methods), but *Rorb* expression differences did (Figure S8F; Spearman's r = 0.27, $p = 3.5 \times 10^{-3}$, Mantel test). Thus, transcriptomic subtypes recapitulate projection and laminar identities, while continuous molecular variation captures part of the fine-scale structural heterogeneity.

Subcellular RNA localization patterns as an additional molecular axis

Beyond gene-expression levels, the super-resolution expansion microscopy used for 2cEASI-FISH allowed precise subcellular localization of single mRNA molecules, including dendritic transcripts (Figure S9A). Using cytoDAPI-based cell and nuclear segmentation, we quantified eight 3D subcellular RNA

(I) Intranuclear enrichment of *Col6a1* relative to *Vglut1* and *Eef2*. Right, example cells displaying corresponding subcellular RNA distributions. Scale bar, 5 μm.
(J) Violin plots of top subRNA-Loc features distinguishing PT from IT neurons. Bottom, representative subcellular RNA distributions (two-sided Wilcoxon rank-sum test). Scale bar, 5 μm.
(K) UMAP based on 240 subRNA-Loc features (STAR Methods), colored by subcellular transcriptomic subtype.
(L) Concordance of subcellular transcriptomic subtypes with projection types shown as a contingency matrix (cell counts). Fisher's exact test.
Statistics are provided in Table S3.

Please cite this article in press as: Zhao et al., Multimodal imaging of gene expression, morphology, and activity of the same neuron, Cell (2026), https://doi.org/10.1016/j.cell.2026.05.041

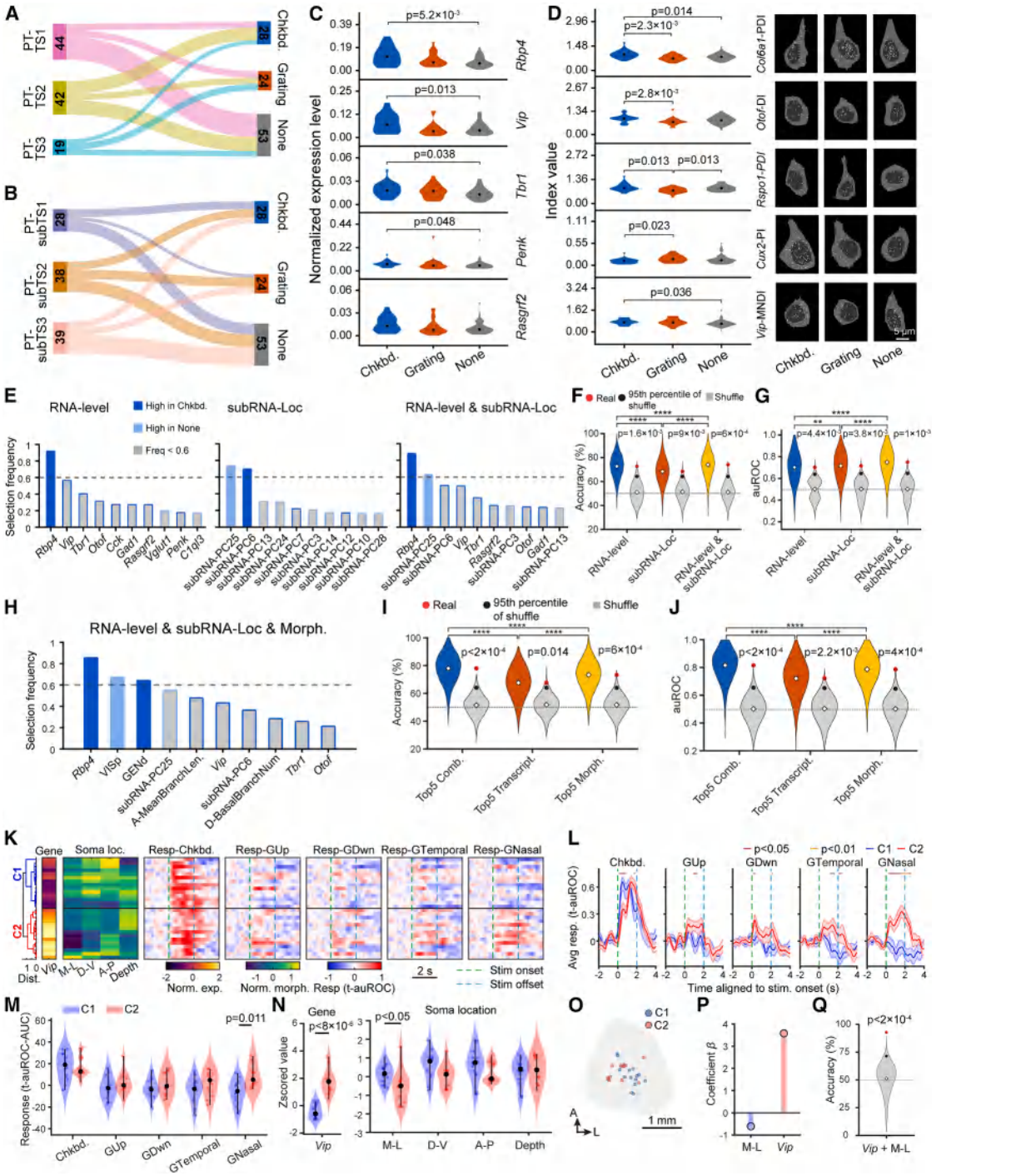

Figure 6. Predicting neuronal function from cellular transcriptomic and morphological features

(A and B) Sankey diagrams linking PT transcriptomic (A) and subcellular transcriptomic (B) subtypes to functional subtypes. Numbers, cell counts.

(C) Normalized expression levels of the top 5 differentially expressed genes (ranked by *p* values for checkerboard vs. none) across functional subtypes. Kruskal-Wallis test followed by Dunn's post hoc test with BH FDR correction.

(D) Violin plots of 5 subRNA-Loc features distinguishing functional subtypes. Right, representative subcellular RNA distributions. Kruskal-Wallis test followed by Dunn's post hoc test with BH FDR correction. Scale bar, 5 μm.

(E) Stability-selection rankings of RNA-level, subRNA-Loc, and combined RNA (RNA-level and subRNA-Loc) features. Dashed line, 60% threshold. Bars are color-coded by enrichment (checkerboard-dominant vs. none).

(legend continued on next page)

Please cite this article in press as: Zhao et al., Multimodal imaging of gene expression, morphology, and activity of the same neuron, Cell (2026), https://doi.org/10.1016/j.cell.2026.05.041

localization (subRNA-Loc) features adopted from previous studies[48,49]: polarization index (PI), dispersion index (DI), peripheral distribution index (PDI), cell edge index (CEI), nuclear edge index (NEI), mean nuclear distance index (MNDI), mean cell distance index (MCDI), and intranuclear index (INI). Across 30 genes, this yielded a 240-feature panel per neuron (STAR Methods).

This analysis revealed gene-specific subcellular localization patterns: relative to *Vglut1* and *Eef2* transcripts, *Cck* transcripts were more polarized (Figure S9B), whereas *Col6a1* transcripts were preferentially nuclear (Figure 5I). Differential analysis identified *Fezf2*-PI, *Bcl6*-PI, *Col6a1*-INI, *Rspo1*-MCDI, and *Dkk3*-INI as the top 5 subRNA-Loc features distinguishing PT from IT neurons (Figure 5J). Unsupervised clustering of subRNA-Loc features defined two subcellular transcriptomic subtypes (subTS1 and subTS2) (Figures 5K and S9C) that also tracked projection identity: PT neurons were enriched in subTS1 (82/92 vs. 105/141, $p = 6.8 \times 10^{-3}$, Fisher's exact test), whereas IT neurons were enriched in subTS2 (Figure 5L; 26/49 vs. 36/141, $p = 6.8 \times 10^{-4}$, Fisher's exact test).

These results establish subcellular transcript localization as an additional spatially resolved molecular axis complementing mRNA expression levels (RNA-level). We therefore treated RNA-level and subRNA-Loc features as two complementary axes of the cellular transcriptomic profile.

Prediction of *in vivo* neuronal functions from cellular transcriptomic profiles

We next examined how *in vivo* functional responses relate to cellular transcriptomic profiles. Because IT functional subtypes were under-represented (Figures S3A and S9D), we focused on the 105 PT neurons. Unsupervised clustering classified these neurons into three transcriptomic subtypes (PT-TS1-3; Figures S9E and S9F) and subcellular transcriptomic subtypes (PT-subTS1-3; Figures S9G and S9H), using RNA-level and subRNA-Loc features, respectively. Although these subtypes aligned well with projection types, their correspondences to functional subtypes were more variable (Figures 6A and 6B), indicating that unsupervised transcriptomic clustering did not fully capture functional diversity.

We therefore applied supervised analyses. Differential analyses of RNA-level features showed that *Rbp4*, *Vip*, *Penk*, and *Tbr1* were significantly higher in checkerboard-dominant than in non-responsive neurons (Figure 6C; all $p\text{adj} < 0.05$; statistics in Table S3). SubRNA-Loc features also showed functional subtype-specific signatures: checkerboard-dominant neurons exhibited significantly higher *Col6a1*-PDI, *Otof*-DI, and *Rspo1*-PDI but lower *Cux2*-PI than grating-dominant neurons; relative to non-responsive neurons, checkerboard-dominant neurons displayed elevated *Col6a1*-PDI and *Vip*-MNDI, whereas grating-dominant neurons showed significantly reduced *Rspo1*-PDI (Figure 6D).

We then trained LassoGLM classifiers to predict functional identities from cellular transcriptomic profiles (STAR Methods). Feature selection identified *Rbp4*, *Vip*, and *Tbr1* as the top RNA-level predictors for distinguishing checkerboard-dominant from non-responsive neurons, with only *Rbp4* exceeding the stability-selection threshold (Figure 6E). The classifier performed significantly above chance (Figures 6F and 6G; accuracy = 72.7% ± 9.5%, $p = 1.6 \times 10^{-3}$; area under the receiver operating characteristic curve [auROC] = 0.70 ± 0.14, $p = 4.4 \times 10^{-3}$; mean ± SD, permutation tests). To balance feature dimensionality, we reduced the 240 subRNA-Loc features to 30 principal components (subRNA-PCs) (Figures S6A and S6B; STAR Methods). A LassoGLM classifier trained on these subRNA-PCs also performed above chance (Figure 6F, accuracy = 68.4% ± 10.2%, $p = 9 \times 10^{-3}$; Figure 6G, auROC = 0.72 ± 0.13, $p = 3.8 \times 10^{-3}$; mean ± SD, permutation tests), with subRNA-PC25 and subRNA-PC6 as key predictors (Figure 6E), dominated by *Tac1*-NEI and *Col6a1*-PDI, respectively (Figure S6B).

Combining RNA-level and subRNA-Loc features further improved prediction performance (Figures 6E–6G; STAR Methods; combined accuracy = 74.1% ± 9.8%, $p = 6 \times 10^{-4}$; combined auROC = 0.75 ± 0.13, $p = 1 \times 10^{-3}$;

(F) Accuracy for models trained on features passing the 60% threshold. Red dots, real accuracies; gray violins, shuffle distributions; black dots, 95th percentile of shuffle; dashed line, 50%. All models exceeded chance (RNA-level, $p = 1.6 \times 10^{-3}$; subRNA-Loc, $p = 9 \times 10^{-3}$; combined, $p = 6 \times 10^{-4}$; permutation test). The combined model outperformed the RNA-level model ($p\text{adj} = 2.10 \times 10^{-5}$) and the subRNA-Loc model ($p\text{adj} = 4.25 \times 10^{-67}$; two-sided Wilcoxon rank-sum test with Bonferroni correction; $^{****}p < 1 \times 10^{-4}$).
(G) auROC for the same models as in (F). All models exceeded chance (RNA-level, $p = 4.4 \times 10^{-3}$; subRNA-Loc, $p = 3.8 \times 10^{-3}$; combined, $p = 1 \times 10^{-3}$; permutation test), and the combined model outperformed the RNA-level model ($p\text{adj} = 3.11 \times 10^{-3}$) and the subRNA-Loc model ($p\text{adj} = 2.67 \times 10^{-27}$; two-sided Wilcoxon rank-sum test with Bonferroni correction; $^{**}p < 0.01$; $^{****}p < 1 \times 10^{-4}$).
(H) Stability-selection ranking when RNA-level, subRNA-Loc, and morphological features were evaluated jointly.
(I and J) Performance (I, accuracy; J, auROC) of models trained on the top 5 features from the combined, transcriptome-only, or morphology-only feature sets. Symbols and statistics as in (F).
(K) Unsupervised clustering of checkerboard-responsive PT neurons into C1 (blue) and C2 (red) using *Vip* expression and soma location. Heatmap shows normalized *Vip* expression, soma location and stimulus-aligned responses (t-auROC) to five visual stimuli. Green/cyan dashed lines, stimulus onset/offset. M-L, medial-lateral; D-V, dorsal-ventral; A-P, anterior-posterior.
(L) Average stimulus-aligned response dynamics (t-auROC; mean ± SEM) for C1 and C2 across five stimuli. Shaded areas, SEM; green/cyan dashed lines, stimulus onset/offset. Top colored bars indicate significant C1 vs. C2 differences (two-sided unpaired *t* test; contiguous significant duration > 200 ms).
(M) Response magnitudes for C1 and C2 across stimuli, quantified as post-onset area under the response curve. Violin plots show distributions; red/blue dots, neurons; black dots, medians; whiskers, value range. Two-sided Wilcoxon rank-sum test with BH FDR correction.
(N) Violin plots of *Vip* expression and soma-location parameters (M-L, D-V, A-P, and depth) for C1 and C2. Plot elements and statistics as in (M).
(O) Spatial distribution of C1 (blue) and C2 (red) somas in a horizontal CCFv3 atlas view. Scale bar, 1 mm.
(P) Logistic regression coefficients (β) for classifying C1 vs. C2 using *Vip* expression and M-L soma position.
(Q) Accuracy of the logistic-regression model in (P), compared with shuffled labels ($p < 2 \times 10^{-4}$). Symbols and statistics as in (F).
Statistics are provided in Table S3.

Please cite this article in press as: Zhao et al., Multimodal imaging of gene expression, morphology, and activity of the same neuron, Cell (2026), https://doi.org/10.1016/j.cell.2026.05.041

mean ± SD, permutation tests; all pairwise $p$adj < 2.2×10^{-5}; statistics in Table S3), indicating that subcellular RNA distribution complements gene-expression levels for decoding neuronal functions. Similar effects were observed in other pairwise comparisons (Figures S6C–S6H), prompting us to test whether adding morphological features could further improve prediction.

Improved prediction of neuronal functions by combining transcriptomic and morphological features

We therefore constructed an integrated feature set comprising 29 RNA-level features, 30 subRNA-PCs, and 38 morphological features (Figure S6A). For the checkerboard-dominant vs. non-responsive comparison, LassoGLM identified *Rbp4* as the only RNA-level predictor, alongside VISp and GENd (geniculate group, dorsal thalamus) as morphological predictors (Figure 6H), largely consistent with the single-modality analyses (Figures 4H and 6E).

To assess modality contributions directly, we trained morphology-only, transcriptome-only, and combined models on the same 105 PT neurons with complete trimodal profiles. To control the number of predictors, we focused on models trained using the top 5 features (Figure 6H). The combined model performed best (Figures 6I and 6J; accuracy = 78% ± 10.3%, auROC = 0.82 ± 0.11, mean ± SD), surpassing the transcriptome-only model (accuracy = 67.6% ± 10.9%, auROC = 0.72 ± 0.13, mean ± SD; both $p$adj < 5.03×10^{-120}, two-sided Wilcoxon rank-sum test with Bonferroni correction) and the morphology-only model (accuracy = 73.3% ± 10.3%, auROC = 0.79 ± 0.11, mean ± SD; both $p$adj < 1.42×10^{-16}, two-sided Wilcoxon rank-sum test with Bonferroni correction). The other two pairwise comparisons showed the same trend (Figures S6I–S6N). In particular, subRNA-PC6 ranked as the top combined predictor for distinguishing checkerboard-dominant from grating-dominant neurons, highlighting subcellular RNA localization as an additional molecular axis for functional prediction. Together, these results underscore the complementary roles of RNA-level, subRNA-Loc, and morphological features in determining neuronal functional specialization and indicate that a single informative gene such as *Rbp4* may serve as an effective marker for functionally distinct neurons.

Vip expression and soma location delineate a PT subtype co-activated by checkerboard and nasal-ward grating stimuli

Among checkerboard-responsive PT neurons, *Vip* expression was significantly enriched (Figure 6C) and ranked among the top RNA-level features for distinguishing these neurons from non-responsive neurons (Figures 6E and 6H). Although *Vip*, *Pvalb*, and *Gad1* are traditionally regarded as inhibitory markers, we detected their expression in a subgroup of excitatory neurons (Figures 5E and S8A).

Motivated by these observations, we asked whether integrating *Vip* expression with spatial coordinates could resolve finer functional subtypes within checkerboard-responsive PT neurons. Because this subgroup was small (n = 28), we focused deliberately on *Vip* transcript levels and soma locations rather than high-dimensional morphological features to ensure robust, experimentally addressable subtyping. Unsupervised hierarchical clustering based on these two variables divided these neurons into C1 and C2 subtypes (Figure 6K). Although both subtypes were robustly activated by checkerboard stimuli, they differed significantly in their responses to nasal-ward-drifting gratings in both response dynamics (Figure 6L; two-sided unpaired t test, contiguous significant duration > 200 ms; STAR Methods) and overall response magnitude (Figure 6M; p = 0.011, two-sided Wilcoxon rank-sum test with BH FDR correction across stimulus conditions).

The C2 subtype exhibited significantly higher *Vip* expression and a more medial soma distribution compared with C1 (Figures 6N and 6O; *Vip*, $p < 8 \times 10^{-6}$; M-L, $p < 0.05$; two-sided Wilcoxon rank-sum test with BH FDR correction across comparisons), indicating that a simple molecular-and-positional signature captures a coherent functional subset. A minimal logistic-regression classifier using only *Vip* expression and medial-lateral (M-L) soma coordinates distinguished C1 from C2 with an accuracy of 92.14% ± 10.99% (mean ± SD), significantly above chance (Figure 6Q; $p < 2 \times 10^{-4}$, permutation test), with *Vip* expression carrying the dominant predictive weight (Figure 6P).

Together, these results identify a *Vglut1*$^+$/*Vip*$^+$ PT neuronal subtype (C2) near the cortical midline that is co-activated by checkerboard stimuli and nasal-ward-drifting gratings and demonstrate how the IMC platform can reduce high-dimensional multimodal data to a small set of experimentally tractable features for targeted follow-up studies.

Functional validation on molecularly defined visual neurons

After identifying higher *Rbp4* expression as a significant predictor for checkerboard-dominant PT neurons, we performed additional *in vivo* functional imaging for validation. We selectively labeled Rbp4-expressing neurons with GCaMP6s in Rbp4-Cre mice via Cre-dependent viral expression (Rbp4-Cre::GCaMP6s mice) (Figure 7A). As a reference, we used Thy1-GCaMP6s mice, which randomly label ~70% of excitatory cortical neurons.[50] EASI-FISH showed that in Rbp4-Cre cortex, *Cre*$^-$/*Vglut1*$^+$ neurons had low-level Rbp4 signal, whereas *Cre*$^+$/*Vglut1*$^+$ neurons exhibited significantly higher *Rbp4* puncta counts (Figure S8G), indicating Cre-dependent enrichment rather than exclusive labeling. This was further supported by cross-dataset analysis using the Allen Brain Cell (ABC) Atlas (Figure S8H; STAR Methods). Unexpectedly, the highest Rbp4-expressing neurons were GCaMP-negative and *Gad1*$^+$, indicating an inhibitory phenotype (Figure S8I) that was also evident in our analysis of the ABC Atlas[51] (Figure S8J). Nevertheless, GCaMP6s in Rbp4-Cre::GCaMP6s mice were primarily expressed in excitatory neurons with intermediate *Rbp4* levels (Figure S8I), and their *Rbp4* expression was significantly higher than that of Thy1-GCaMP6s$^+$ neurons (Figure 7B).

We next performed functional imaging in 6 VISp FOVs localized by intrinsic signal optical imaging (Figures 7C and 7D; STAR Methods), sampling 3 imaging planes at depths of 400–550 μm below the dura. Given the substantially larger number of neurons (n = 3,485) than in the trimodal dataset, we categorized responses into four types for higher-resolution

Please cite this article in press as: Zhao et al., Multimodal imaging of gene expression, morphology, and activity of the same neuron, Cell (2026), https://doi.org/10.1016/j.cell.2026.05.041

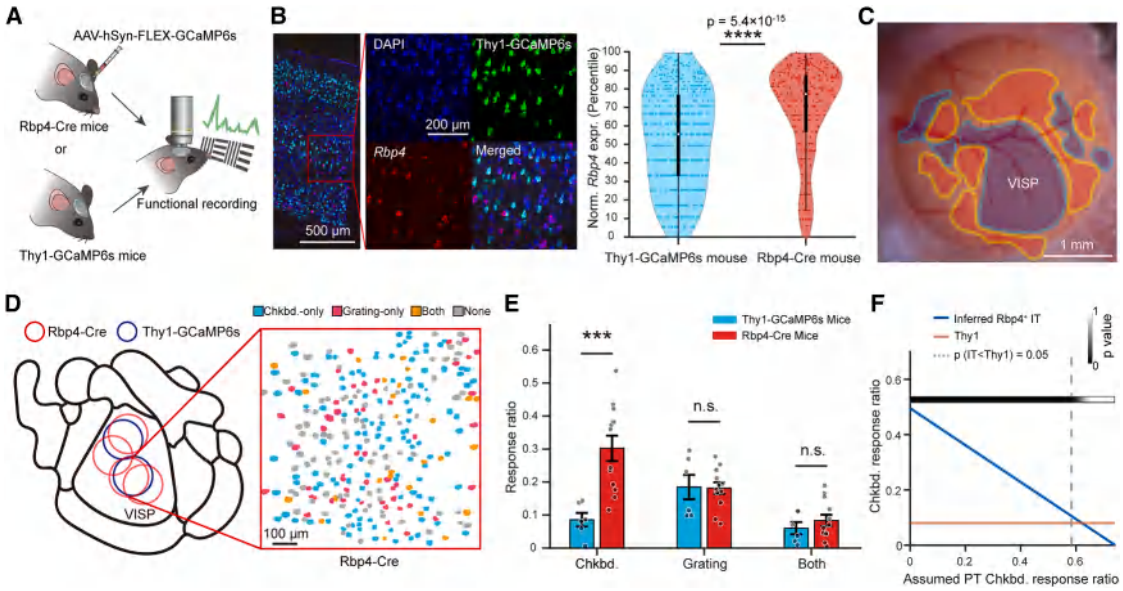

Figure 7. Validation of visual responses in molecularly defined neurons

(A) Functional imaging in Rbp4-Cre mice with virally induced GCaMP6s expression (AAV-hSyn-FLEX-GCaMP6s) and Thy1-GCaMP6s control mice.

(B) *Rbp4* expression in GCaMP6s-labeled neurons from Thy1-GCaMP6s and Rbp4-Cre::GCaMP6s mice. Left, representative EASI-FISH images showing *Rbp4* expression in Thy1-GCaMP6s$^+$ neurons; scale bars, 500 µm (overview image) and 200 µm (enlarged views). Right, percentile distributions of *Rbp4* puncta counts in GCaMP6s$^+$ neurons from both lines ($p = 5.4 \times 10^{-15}$, two-sided Wilcoxon rank-sum test; ****$p < 1 \times 10^{-4}$).

(C) Representative image of visual areas identified by intrinsic signal optical imaging. Scale bar, 1 mm.

(D) 6 VISp FOVs imaged in Rbp4-Cre and Thy1-GCaMP6s mice, and 292 neurons color-coded by functional type in a representative FOV imaged in an Rbp4-Cre mouse. Functional imaging was performed at three depths per FOV (Table S1). Scale bar, 100 µm.

(E) Proportions of visually responsive neuronal types in Rbp4-Cre mice (two mice, $n = 12$ imaging planes) and Thy1-GCaMP6s mice (two mice, $n = 6$ imaging planes). Rbp4-Cre mice had a higher fraction of checkerboard-selective neurons ($p = 4.3 \times 10^{-4}$, two-sided Wilcoxon rank-sum test), but not grating-selective ($p = 0.89$) or dually responsive neurons ($p = 0.44$); two-sided Wilcoxon rank-sum test, ***$p < 0.001$; n.s., not significant. Data are mean ± SEM.

(F) Statistical significance (Fisher's exact test; STAR Methods) for the hypothesis that *Rbp4*$^+$ IT neurons exhibit a higher checkerboard-responsive rate than Thy1-GCaMP6s neurons, plotted against the presumed checkerboard-responsive rate of *Rbp4*$^+$ PT neurons. Dashed line, $p = 0.05$. The *Rbp4*$^+$ IT:PT ratio was assumed to be 3:2.[41]

Statistics are provided in Table S3.

analysis: checkerboard-only, grating-only, checkerboard & grating, and non-responsive (STAR Methods). The percentage of checkerboard-only neurons was significantly higher in Rbp4-Cre::GCaMP6s mice than in Thy1-GCaMP6s mice (Figure 7E, $p = 4.3 \times 10^{-4}$, two-sided Wilcoxon rank-sum test).

Because Rbp4-Cre mice label both PT and IT neurons,[52,53] we asked whether *Rbp4* expression predicted checkerboard responsiveness in both types. As shown in Figure 7F, if the percentage of checkerboard-responsive *Rbp4*$^+$ PT neurons was lower than 58.4%, then the percentage of checkerboard-responsive *Rbp4*$^+$ IT neurons was significantly higher than that in Thy1-GCaMP6s$^+$ neurons ($p < 0.05$, Fisher's exact test) (STAR Methods). These results not only support our trimodal integration findings in PT neurons but also suggest that *Rbp4* is a general molecular marker for VISp neurons with a high probability of checkerboard responsiveness.

DISCUSSION

Dissecting the brain at the single-neuron level has long been a central goal in neuroscience. Recent technological advances have enabled extensive investigation of three neuronal modalities at the single-cell level: physiological properties, local and long-range connectivity, and gene-expression profiles. Integrating these modalities represents an emerging frontier for deciphering neuronal functional specialization.[3] However, most existing approaches still rely on separate technical pipelines for each modality. Two key challenges are preserving tissue and molecular integrity for sequential characterization and identifying the same neurons across modalities. Optical imaging is well suited to these requirements, as it has enabled pairwise bimodal integration of these modalities.[4–12,54] Here, we extend these bimodal strategies to trimodal integration at the single-neuron level.

A key component of our IMC platform is whole-brain morphological characterization, which requires continuous high-resolution imaging across a large volume. Although various strategies have been developed recently to image the entire brain,[28,55–63] they often require trade-offs among tissue integrity, sample processing complexity, imaging resolution and speed, automation, and post-imaging processing. To enable subsequent gene-expression profiling and maximize the success rate of trimodal integration, we optimized imaging resolution, tissue integrity, efficient sample processing, and procedural reliability. We

Please cite this article in press as: Zhao et al., Multimodal imaging of gene expression, morphology, and activity of the same neuron, Cell (2026), https://doi.org/10.1016/j.cell.2026.05.041

developed MP-TPM to image intact cleared brains with greater tolerance to imperfect sample transparency and RI uniformity, thereby enabling a simple organic solvent-based whole-brain clearing method that preserves molecular integrity. Together, these features form the foundation of the IMC platform. While we intentionally prioritized imaging sensitivity over speed by employing long pixel integration times, the overall workflow remains simple, robust, and amenable to automation and scaling.

Compared with Patch-seq,[3,20] a cutting-edge trimodal approach most commonly combining local morphological reconstruction, in-slice electrophysiology, and post-patching single-cell RNA sequencing, our platform provides *in vivo* optical functional readouts (currently Ca^{2+} imaging but readily extensible to voltage imaging), intact whole-brain projection patterns, and *in situ* gene profiles from the same neuron. Patch-seq excels in temporal resolution and transcriptomic depth, whereas our IMC platform links behaviorally relevant *in vivo* function with brain-wide axonal projections and subcellular gene-expression patterns.

Subcellular mRNA localization is important for compartment-specific translation in neurons with highly polarized structures. Previous studies have established that subcellular RNA localization is tightly coupled to neuronal activity[64,65] and that developing projection neurons exhibit type-specific local transcriptomes in growth cones.[66,67] However, integrated analysis in the adult cortex connecting subcellular transcript distribution with dendrite/axon projection patterns and neuronal function remains technically challenging. Our IMC platform addresses this challenge by integrating subcellular RNA localization with morphological and functional identities. For example, we identified PT- and IT-specific subcellular transcript localization patterns, providing an entry point for studying how subcellularly localized transcripts shape neuronal morphology and function.

We demonstrated the IMC platform's capabilities by characterizing mouse VISp cortical projection neurons. We identified morphological and transcriptomic features associated with differential visual responses. For example, grating-dominant PT neurons exhibited more extensive axonal projections within VISp than checkerboard-dominant PT neurons, suggesting that greater information transformation and finer feature extraction occur with grating stimuli.[68] Furthermore, checkerboard-dominant PT neurons exhibited higher *Rbp4* expression than non-responsive PT neurons, a result later confirmed through larger-scale functional characterization of *Rbp4*$^{+}$ neurons. These findings demonstrate the effectiveness and reliability of our trimodal approach for exploring the multimodal basis of neuronal functional specialization.

Beyond linking multimodal features to neuronal activity, the IMC platform further enables the discovery of previously unrecognized functional subtypes using a minimal set of experimentally tractable features. By integrating *Vip* expression with soma location, we delineated a distinct PT subtype (C2) co-activated by high-contrast checkerboards and nasal-ward drifting gratings (Figures 6K–6Q). Given that PT neurons provide major cortical outputs to subcortical motor and reflex centers, the C2 subtype may represent a specialized, molecularly defined visuomotor channel relevant to visually driven defensive behavior.[69] Future work should isolate this population, map its downstream connectivity, and assess its causal contribution to behavior. More broadly, this example illustrates how trimodal measurements in the same identified neurons can distill exploratory correlations into concise, testable hypotheses.

Beyond extending trimodal characterization to additional neuronal types and brain regions, the IMC platform can bridge growing unimodal and bimodal datasets by aligning informative multimodal features[23] and be combined with diverse behavioral paradigms to link task-specific computations to circuit architecture and molecular identity. In addition, it allows systematic cross-species comparisons to reveal how homologous molecularly defined neuronal types diverge in projection patterns and behavioral coding. By delivering authentic multimodal datasets from the same neurons, our platform also provides ground-truth resources for benchmarking emerging analytical approaches in multimodal data integration.[70] Together, these capabilities position IMC as a versatile approach for unifying functional, structural, and molecular insights, thereby fostering a multiscale mechanistic understanding of brain function in both basic and translational neuroscience.

Limitations of the study

A primary limitation of this work is throughput. First, functional characterization throughput is lower than in conventional Ca^{2+} imaging because sparse labeling is required for subsequent axon tracing. 2D imaging over a limited FOV using traditional TPM can only capture a few sparsely labeled neurons at once. Sequential imaging across multiple depths and FOVs is time-consuming and labor-intensive, limiting both the number of visual stimuli tested per neuron and the number of neurons functionally characterized per brain. Future large-FOV volumetric functional imaging could improve throughput. Second, gene-expression profiling via 2cEASI-FISH is time-intensive. Here, we performed five sequential rounds to detect 30 RNAs. Sequential detection was deliberately chosen in this proof-of-principle study to provide high fault tolerance for our precious trimodal samples and to avoid optical crowding and error-prone cross-cycle 3D registration associated with emerging highly multiplexed 3D spatial transcriptomic methods.[71,72] Although practical time constraints limited the number of FISH rounds, 2cEASI-FISH showed high mRNA retention comparable to the original EASI-FISH (Figure S7B), is theoretically scalable to dozens of rounds, and doubles the per-round detection capacity of the original EASI-FISH and cycleHCR.[39] Full automation[39] and cross-round barcoding[71,72] could further increase throughput. Alternatively, future implementations could leverage comprehensive public single-cell transcriptomic datasets to focus on a small, highly informative panel of marker genes.

A second limitation concerns sampling bias. Despite stochastic viral infection for sparse labeling, neuronal types were not uniformly sampled. For instance, CT neurons were absent from our trimodal dataset, likely because their deep soma locations hindered Ca^{2+} imaging. Additionally, PT neurons predominated over IT neurons, possibly reflecting viral tropism at low titers.[73] Future transgenic sparse labeling strategies may provide more uniform sampling of diverse neuronal types at higher throughput, whereas enhancer-driven AAVs could offer an effective alternative for targeted expression in specific neuronal subtypes.

Finally, the relatively small sample size of this initial study motivated the use of conservative linear models to enhance interpretability and mitigate overfitting. As throughput and sample sizes increase, emerging multimodal analysis methods, including AI-based integration and representation learning, should more effectively uncover cross-modal associations and latent features that jointly capture molecular, morphological, and functional attributes.

RESOURCE AVAILABILITY

Lead contact

Further information and requests for resources and reagents should be directed to and will be fulfilled by the lead contact, Shengjin Xu (sxu@ion.ac.cn).

Materials availability

This study did not generate any unique reagents.

Data and code availability

Processed trimodal data are available at 10.12412/BSDC.1760411296.20002 and an interactive website (https://mouse.digital-brain.cn/trimodal). Custom LabVIEW, MATLAB, and R codes for data acquisition and analysis are available on GitHub: https://github.com/WKLabION/Trimodal-Data-and-Analysis and https://github.com/Saintgene-Xu-lab/2cEASI-FISH-analysis.

ACKNOWLEDGMENTS

We thank Mu-ming Poo, Yangang Sun, and Zengcai Guo for offering insightful critiques of our manuscript. We thank J. Cao for mice care. We thank Jun Yan and Le Gao for assistance and suggestions on structural reconstruction and structural data analysis. This research was supported by Brain Science and Brain-like Intelligence Technology—National Science and Technology Major Project (2021ZD0204400 to S.X.; 2021ZD0204500 to K.W.), the National Natural Science Foundation of China (32125020 to K.W.; 32371072 to S.X.; 32321003 to K.W. and S.X.; 32300936 to L.C.), the Shanghai Committee of Science and Technology, China (22JC1403100 to K.W. and S.X.), the Strategic Priority Research Program of the Chinese Academy of Sciences (XDB1010102 to K.W.), and the China Postdoctoral Science Foundation (2023M743609 and BX20240389 to L.B.).

AUTHOR CONTRIBUTIONS

K.W. and S.X. conceptualized the project. Z.S., Y. Zhao, and Y. Zhang developed mice surgery. Z.S. and Y. Zhao performed functional imaging under the supervision of N.X. and K.W. Z.S., P.Y., and L.B. developed brain-clearing methods. L.C., Z.S., and P.Y. built the MP-TPM and conducted whole mouse brain imaging. X.L. and L.G. developed 2cEASI-FISH. X.L. performed gene-expression profiling and data analysis under the supervision of S.X. Y. Zhao and X.S. conducted registrations of brains into a common brain atlas under the supervision of X.W. Y. Zhao and Z.S. performed functional and morphological characterizations on neurons. X.L., C.J., L.Q., W.D., X.Z., and T.Z. built the interactive website. Y. Zhao, Z.S., and X.L. performed multi-modal integration analysis. K.W., S.X., Y. Zhao, Z.S., and X.L. wrote the manuscript with inputs from all authors. K.W., S.X., and N.X. supervised the project.

DECLARATION OF INTERESTS

K.W., L.C., Y. Zhao, Z.S., and L.B. are listed as inventors on Chinese patent no. 2024113962145. S.X., X.L., C.C., and L.G. are listed as inventors on Chinese patent no. 2025115789653.

STAR★METHODS

Detailed methods are provided in the online version of this paper and include the following:

SUPPLEMENTAL INFORMATION

Supplemental information can be found online at https://doi.org/10.1016/j.cell.2026.05.041.

Received: October 22, 2025
Revised: March 10, 2026
Accepted: May 27, 2026

REFERENCES

1. Luo, L., Callaway, E.M., and Svoboda, K. (2008). Genetic Dissection of Neural Circuits. Neuron *57*, 634–660. https://doi.org/10.1016/j.neuron.2008.01.002.
2. Zeng, H. (2022). What is a cell type and how to define it? Cell *185*, 2739–2755. https://doi.org/10.1016/j.cell.2022.06.031.
3. Arkhipov, A., Da Costa, N., De Vries, S., Bakken, T., Bennett, C., Bernard, A., Berg, J., Buice, M., Collman, F., Daigle, T., et al. (2025). Integrating multimodal data to understand cortical circuit architecture and function. Nat. Neurosci. *28*, 717–730. https://doi.org/10.1038/s41593-025-01904-7.
4. Xu, S., Yang, H., Menon, V., Lemire, A.L., Wang, L., Henry, F.E., Turaga, S.C., and Sternson, S.M. (2020). Behavioral state coding by molecularly

defined paraventricular hypothalamic cell type ensembles. Science *370*, eabb2494. https://doi.org/10.1126/science.abb2494.

5. Condylis, C., Ghanbari, A., Manjrekar, N., Bistrong, K., Yao, S., Yao, Z., Nguyen, T.N., Zeng, H., Tasic, B., and Chen, J.L. (2022). Dense functional and molecular readout of a circuit hub in sensory cortex. Science *375*, eabl5981. https://doi.org/10.1126/science.abl5981.
6. Liu, Y., Savier, E.L., DePiero, V.J., Chen, C., Schwalbe, D.C., Abraham-Fan, R.-J., Chen, H., Campbell, J.N., and Cang, J. (2023). Mapping visual functions onto molecular cell types in the mouse superior colliculus. Neuron *111*, 1876–1886. https://doi.org/10.1016/j.neuron.2023.03.036.
7. Bugeon, S., Duffield, J., Dipoppa, M., Ritoux, A., Prankerd, I., Nicoloutsopoulos, D., Orme, D., Shinn, M., Peng, H., Forrest, H., et al. (2022). A transcriptomic axis predicts state modulation of cortical interneurons. Nature *607*, 330–338. https://doi.org/10.1038/s41586-022-04915-7.
8. Lovett-Barron, M., Andalman, A.S., Allen, W.E., Vesuna, S., Kauvar, I., Burns, V.M., and Deisseroth, K. (2017). Ancestral Circuits for the Coordinated Modulation of Brain State. Cell *171*, 1411–1423. https://doi.org/10.1016/j.cell.2017.10.021.
9. Kerlin, A.M., Andermann, M.L., Berezovskii, V.K., and Reid, R.C. (2010). Broadly Tuned Response Properties of Diverse Inhibitory Neuron Subtypes in Mouse Visual Cortex. Neuron *67*, 858–871. https://doi.org/10.1016/j.neuron.2010.08.002.
10. Wang, M., Liu, K., Pan, J., Li, J., Sun, P., Zhang, Y., Li, L., Guo, W., Xin, Q., Zhao, Z., et al. (2022). Brain-wide projection reconstruction of single functionally defined neurons. Nat. Commun. *13*, 1531. https://doi.org/10.1038/s41467-022-29229-0.
11. Zhou, W., Ke, S., Li, W., Yuan, J., Li, X., Jin, R., Jia, X., Jiang, T., Dai, Z., He, G., et al. (2022). Mapping the Function of Whole-Brain Projection at the Single Neuron Level. Adv. Sci. (Weinh) *9*, e2202553. https://doi.org/10.1002/advs.202202553.
12. Li, X., Du, Y., Huang, J.-F., Li, W.-W., Song, W., Fan, R.-N., Zhou, H., Jiang, T., Lu, C.-G., Guan, Z., et al. (2024). Link Brain-Wide Projectome to Neuronal Dynamics in the Mouse Brain. Neurosci. Bull. *40*, 1621–1634. https://doi.org/10.1007/s12264-024-01232-z.
13. Bock, D.D., Lee, W.-C.A., Kerlin, A.M., Andermann, M.L., Hood, G., Wetzel, A.W., Yurgenson, S., Soucy, E.R., Kim, H.S., and Reid, R.C. (2011). Network anatomy and in vivo physiology of visual cortical neurons. Nature *471*, 177–182. https://doi.org/10.1038/nature09802.
14. The MICrONS Consortium (2025). Functional connectomics spanning multiple areas of mouse visual cortex. Nature *640*, 435–447. https://doi.org/10.1038/s41586-025-08790-w.
15. Ding, Z., Fahey, P.G., Papadopoulos, S., Wang, E.Y., Celii, B., Papadopoulos, C., Chang, A., Kunin, A.B., Tran, D., Fu, J., et al. (2025). Functional connectomics reveals general wiring rule in mouse visual cortex. Nature *640*, 459–469. https://doi.org/10.1038/s41586-025-08840-3.
16. Kuan, A.T., Bondanelli, G., Driscoll, L.N., Han, J., Kim, M., Hildebrand, D.G.C., Graham, B.J., Wilson, D.E., Thomas, L.A., Panzeri, S., et al. (2024). Synaptic wiring motifs in posterior parietal cortex support decision-making. Nature *627*, 367–373. https://doi.org/10.1038/s41586-024-07088-7.
17. Jiao, Z., Gao, T., Wang, X., Wang, A., Ma, Y., Feng, L., Gao, L., Gou, L., Zhang, W., Biglari, N., et al. (2025). Projectome-based characterization of hypothalamic peptidergic neurons in male mice. Nat. Neurosci. *28*, 1073–1088. https://doi.org/10.1038/s41593-025-01919-0.
18. Kebschull, J.M., Garcia Da Silva, P., Reid, A.P., Peikon, I.D., Albeanu, D.F., and Zador, A.M. (2016). High-Throughput Mapping of Single-Neuron Projections by Sequencing of Barcoded RNA. Neuron *91*, 975–987. https://doi.org/10.1016/j.neuron.2016.07.036.
19. Yuan, L., Chen, X., Zhan, H., Henry, G.L., and Zador, A.M. (2024). Massive multiplexing of spatially resolved single neuron projections with axonal BARseq. Nat. Commun. *15*, 8371. https://doi.org/10.1038/s41467-024-52756-x.
20. Cadwell, C.R., Palasantza, A., Jiang, X., Berens, P., Deng, Q., Yilmaz, M., Reimer, J., Shen, S., Bethge, M., Tolias, K.F., et al. (2016). Electrophysiological, transcriptomic and morphologic profiling of single neurons using Patch-seq. Nat. Biotechnol. *34*, 199–203. https://doi.org/10.1038/nbt.3445.
21. Fuzik, J., Zeisel, A., Máté, Z., Calvigioni, D., Yanagawa, Y., Szabó, G., Linnarsson, S., and Harkany, T. (2016). Integration of electrophysiological recordings with single-cell RNA-seq data identifies neuronal subtypes. Nat. Biotechnol. *34*, 175–183. https://doi.org/10.1038/nbt.3443.
22. Ge, Q., Yang, J., Huang, F., Dai, X., Chen, C., Guo, J., Wang, M., Zhu, M., Shao, Y., Xia, Y., et al. (2025). Multimodal single-cell analyses reveal molecular markers of neuronal senescence in human drug-resistant epilepsy. J. Clin. Investig. *135*, e188942. https://doi.org/10.1172/JCI188942.
23. Sorensen, S.A., Gouwens, N.W., Wang, Y., Mallory, M., Budzillo, A., Dalley, R., Lee, B., Gliko, O., Kuo, H.C., Kuang, X., et al. (2023). Connecting single-cell transcriptomes to projectomes in mouse visual cortex. Preprint at bioRxiv. 2023.11.25.568393. https://doi.org/10.1101/2023.11.25.568393.
24. Winnubst, J., Bas, E., Ferreira, T.A., Wu, Z., Economo, M.N., Edson, P., Arthur, B.J., Bruns, C., Rokicki, K., Schauder, D., et al. (2019). Reconstruction of 1,000 Projection Neurons Reveals New Cell Types and Organization of Long-Range Connectivity in the Mouse Brain. Cell *179*, 268–281. https://doi.org/10.1016/j.cell.2019.07.042.
25. Gao, L., Liu, S., Gou, L., Hu, Y., Liu, Y., Deng, L., Ma, D., Wang, H., Yang, Q., Chen, Z., et al. (2022). Single-neuron projectome of mouse prefrontal cortex. Nat. Neurosci. *25*, 515–529. https://doi.org/10.1038/s41593-022-01041-5.
26. Wang, Y., Eddison, M., Fleishman, G., Weigert, M., Xu, S., Wang, T., Rokicki, K., Goina, C., Henry, F.E., Lemire, A.L., et al. (2021). EASI-FISH for thick tissue defines lateral hypothalamus spatio-molecular organization. Cell *184*, 6361–6377. https://doi.org/10.1016/j.cell.2021.11.024.
27. Li, A., Gong, H., Zhang, B., Wang, Q., Yan, C., Wu, J., Liu, Q., Zeng, S., and Luo, Q. (2010). Micro-Optical Sectioning Tomography to Obtain a High-Resolution Atlas of the Mouse Brain. Science *330*, 1404–1408. https://doi.org/10.1126/science.1191776.
28. Economo, M.N., Clack, N.G., Lavis, L.D., Gerfen, C.R., Svoboda, K., Myers, E.W., and Chandrashekar, J. (2016). A platform for brain-wide imaging and reconstruction of individual neurons. eLife *5*, e10566. https://doi.org/10.7554/eLife.10566.
29. Weiss, K.R., Voigt, F.F., Shepherd, D.P., and Huisken, J. (2021). Tutorial: practical considerations for tissue clearing and imaging. Nat. Protoc. *16*, 2732–2748. https://doi.org/10.1038/s41596-021-00502-8.
30. Kim, K.H., Buehler, C., Bahlmann, K., Ragan, T., Lee, W.-C.A., Nedivi, E., Heffer, E.L., Fantini, S., and So, P.T.C. (2007). Multifocal multiphoton microscopy based on multianode photomultiplier tubes. Opt. Express *15*, 11658–11678. https://doi.org/10.1364/OE.15.011658.
31. Rumyantsev, O.I., Lecoq, J.A., Hernandez, O., Zhang, Y., Savall, J., Chrapkiewicz, R., Li, J., Zeng, H., Ganguli, S., and Schnitzer, M.J. (2020). Fundamental bounds on the fidelity of sensory cortical coding. Nature *580*, 100–105. https://doi.org/10.1038/s41586-020-2130-2.
32. Harris, J.A., Mihalas, S., Hirokawa, K.E., Whitesell, J.D., Choi, H., Bernard, A., Bohn, P., Caldejon, S., Casal, L., Cho, A., et al. (2019). Hierarchical organization of cortical and thalamic connectivity. Nature *575*, 195–202. https://doi.org/10.1038/s41586-019-1716-z.
33. Oh, S.W., Harris, J.A., Ng, L., Winslow, B., Cain, N., Mihalas, S., Wang, Q., Lau, C., Kuan, L., Henry, A.M., et al. (2014). A mesoscale connectome of the mouse brain. Nature *508*, 207–214. https://doi.org/10.1038/nature13186.
34. Wang, Q., Ding, S.-L., Li, Y., Royall, J., Feng, D., Lesnar, P., Graddis, N., Naeemi, M., Facer, B., Ho, A., et al. (2020). The Allen Mouse Brain Common Coordinate Framework: A 3D Reference Atlas. Cell *181*, 936–953. https://doi.org/10.1016/j.cell.2020.04.007.

35. Shepherd, G.M.G. (2013). Corticostriatal connectivity and its role in disease. Nat. Rev. Neurosci. *14*, 278–291. https://doi.org/10.1038/nrn3469.

36. Peng, H., Xie, P., Liu, L., Kuang, X., Wang, Y., Qu, L., Gong, H., Jiang, S., Li, A., Ruan, Z., et al. (2021). Morphological diversity of single neurons in molecularly defined cell types. Nature *598*, 174–181. https://doi.org/10.1038/s41586-021-03941-1.

37. Gao, L., Liu, S., Wang, Y., Wu, Q., Gou, L., and Yan, J. (2023). Single-neuron analysis of dendrites and axons reveals the network organization in mouse prefrontal cortex. Nat. Neurosci. *26*, 1111–1126. https://doi.org/10.1038/s41593-023-01339-y.

38. Meinshausen, N., and Bühlmann, P. (2010). Stability Selection. J. R. Stat. Soc. B *72*, 417–473. https://doi.org/10.1111/j.1467-9868.2010.00740.x.

39. Gandin, V., Kim, J., Yang, L.-Z., Lian, Y., Kawase, T., Hu, A., Rokicki, K., Fleishman, G., Tillberg, P., Castrejon, A.A., et al. (2025). Deep-tissue transcriptomics and subcellular imaging at high spatial resolution. Science *388*, eadq2084. https://doi.org/10.1126/science.adq2084.

40. Yao, Z., van Velthoven, C.T.J. van, Nguyen, T.N., Goldy, J., Sedeno-Cortes, A.E., Baftizadeh, F., Bertagnolli, D., Casper, T., Chiang, M., Crichton, K., et al. (2021). A taxonomy of transcriptomic cell types across the isocortex and hippocampal formation. Cell *184*, 3222–3241. https://doi.org/10.1016/j.cell.2021.04.021.

41. Tasic, B., Yao, Z., Graybuck, L.T., Smith, K.A., Nguyen, T.N., Bertagnolli, D., Goldy, J., Garren, E., Economo, M.N., Viswanathan, S., et al. (2018). Shared and distinct transcriptomic cell types across neocortical areas. Nature *563*, 72–78. https://doi.org/10.1038/s41586-018-0654-5.

42. Sylwestrak, E.L., Rajasethupathy, P., Wright, M.A., Jaffe, A., and Deisseroth, K. (2016). Multiplexed Intact-Tissue Transcriptional Analysis at Cellular Resolution. Cell *164*, 792–804. https://doi.org/10.1016/j.cell.2016.01.038.

43. Muñoz-Castañeda, R., Zingg, B., Matho, K.S., Chen, X., Wang, Q., Foster, N.N., Li, A., Narasimhan, A., Hirokawa, K.E., Huo, B., et al. (2021). Cellular anatomy of the mouse primary motor cortex. Nature *598*, 159–166. https://doi.org/10.1038/s41586-021-03970-w.

44. Zhang, M., Eichhorn, S.W., Zingg, B., Yao, Z., Cotter, K., Zeng, H., Dong, H., and Zhuang, X. (2021). Spatially resolved cell atlas of the mouse primary motor cortex by MERFISH. Nature *598*, 137–143. https://doi.org/10.1038/s41586-021-03705-x.

45. Sun, Y.-C., Chen, X., Fischer, S., Lu, S., Zhan, H., Gillis, J., and Zador, A.M. (2021). Integrating barcoded neuroanatomy with spatial transcriptional profiling enables identification of gene correlates of projections. Nat. Neurosci. *24*, 873–885. https://doi.org/10.1038/s41593-021-00842-4.

46. Gil-Sanz, C., Espinosa, A., Fregoso, S.P., Bluske, K.K., Cunningham, C.L., Martinez-Garay, I., Zeng, H., Franco, S.J., and Müller, U. (2015). Lineage Tracing Using Cux2-Cre and Cux2-CreERT2 Mice. Neuron *86*, 1091–1099. https://doi.org/10.1016/j.neuron.2015.04.019.

47. Alcamo, E.A., Chirivella, L., Dautzenberg, M., Dobreva, G., Fariñas, I., Grosschedl, R., and McConnell, S.K. (2008). Satb2 Regulates Callosal Projection Neuron Identity in the Developing Cerebral Cortex. Neuron *57*, 364–377. https://doi.org/10.1016/j.neuron.2007.12.012.

48. Imbert, A., Ouyang, W., Safieddine, A., Coleno, E., Zimmer, C., Bertrand, E., Walter, T., and Mueller, F. (2022). FISH-quant v2: a scalable and modular tool for smFISH image analysis. RNA *28*, 786–795. https://doi.org/10.1261/rna.079073.121.

49. Park, H.Y., Trcek, T., Wells, A.L., Chao, J.A., and Singer, R.H. (2012). An Unbiased Analysis Method to Quantify mRNA Localization Reveals Its Correlation with Cell Motility. Cell Rep. *1*, 179–184. https://doi.org/10.1016/j.celrep.2011.12.009.

50. Dana, H., Chen, T.-W., Hu, A., Shields, B.C., Guo, C., Looger, L.L., Kim, D.S., and Svoboda, K. (2014). Thy1-GCaMP6 Transgenic Mice for Neuronal Population Imaging In Vivo. PLoS One *9*, e108697. https://doi.org/10.1371/journal.pone.0108697.

51. Yao, Z., van Velthoven, C.T.J., Kunst, M., Zhang, M., McMillen, D., Lee, C., Jung, W., Goldy, J., Abdelhak, A., Aitken, M., et al. (2023). A high-resolution transcriptomic and spatial atlas of cell types in the whole mouse brain. Nature *624*, 317–332. https://doi.org/10.1038/s41586-023-06812-z.

52. Liu, Y., Bech, P., Tamura, K., Délez, L.T., Crochet, S., and Petersen, C.C.H. (2024). Cell class-specific long-range axonal projections of neurons in mouse whisker-related somatosensory cortices. eLife *13*, RP97602. https://doi.org/10.7554/eLife.97602.

53. Gerfen, C.R., Paletzki, R., and Heintz, N. (2013). GENSAT BAC Cre-Recombinase Driver Lines to Study the Functional Organization of Cerebral Cortical and Basal Ganglia Circuits. Neuron *80*, 1368–1383. https://doi.org/10.1016/j.neuron.2013.10.016.

54. Ferreira, T.A., Eddison, M., Copeland, M., Lay, M.L., Weldon, M., Baka, J., Tenshaw, E., Stark, A.K., Schauder, D., Olbris, D.J., et al. (2025). Discovery of neuronal cell types by pairing whole cell reconstructions with RNA expression profiles. Preprint at bioRxiv. https://doi.org/10.1101/2024.12.30.630829.

55. Glaser, A., Chandrashekar, J., Vasquez, S., Arshadi, C., Javeri, R., Ouellette, N., Jiang, X., Baka, J., Kovacs, G., Woodard, M., et al. (2025). Expansion-assisted selective plane illumination microscopy for nanoscale imaging of centimeter-scale tissues. eLife *12*, RP91979. https://doi.org/10.7554/eLife.91979.

56. Chen, Y., Li, X., Zhang, D., Wang, C., Feng, R., Li, X., Wen, Y., Xu, H., Zhang, X.S., Yang, X., et al. (2020). A Versatile Tiling Light Sheet Microscope for Imaging of Cleared Tissues. Cell Rep. *33*, 108349. https://doi.org/10.1016/j.celrep.2020.108349.

57. Dodt, H.-U., Leischner, U., Schierloh, A., Jährling, N., Mauch, C.P., Deininger, K., Deussing, J.M., Eder, M., Zieglgänsberger, W., and Becker, K. (2007). Ultramicroscopy: three-dimensional visualization of neuronal networks in the whole mouse brain. Nat. Methods *4*, 331–336. https://doi.org/10.1038/nmeth1036.

58. Glaser, A.K., Bishop, K.W., Barner, L.A., Susaki, E.A., Kubota, S.I., Gao, G., Serafin, R.B., Balaram, P., Turschak, E., Nicovich, P.R., et al. (2022). A hybrid open-top light-sheet microscope for versatile multi-scale imaging of cleared tissues. Nat. Methods *19*, 613–619. https://doi.org/10.1038/s41592-022-01468-5.

59. Tang, L., Wang, J., Ding, J., Sun, J., Chen, X., Shen, Q., Song, R., Cao, P., Gong, R., Xu, F., et al. (2025). Curved light sheet microscopy for centimetre-scale cleared tissue imaging. Nat. Photon. *19*, 577–584. https://doi.org/10.1038/s41566-025-01659-4.

60. Xu, F., Shen, Y., Ding, L., Yang, C.-Y., Tan, H., Wang, H., Zhu, Q., Xu, R., Wu, F., Xiao, Y., et al. (2021). High-throughput mapping of a whole rhesus monkey brain at micrometer resolution. Nat. Biotechnol. *39*, 1521–1528. https://doi.org/10.1038/s41587-021-00986-5.

61. Zhang, Z., Yao, X., Yin, X., Ding, Z., Huang, T., Huo, Y., Ji, R., Peng, H., and Guo, Z.V. (2021). Multi-Scale Light-Sheet Fluorescence Microscopy for Fast Whole Brain Imaging. Front. Neuroanat. *15*, 732464. https://doi.org/10.3389/fnana.2021.732464.

62. Voigt, F.F., Kirschenbaum, D., Platonova, E., Pagès, S., Campbell, R.A.A., Kastli, R., Schaettin, M., Egolf, L., Van Der Bourg, A., Bethge, P., et al. (2019). The mesoSPIM initiative: open-source light-sheet microscopes for imaging cleared tissue. Nat. Methods *16*, 1105–1108. https://doi.org/10.1038/s41592-019-0554-0.

63. Qi, X., Muñoz-Castañeda, R., Yue, Y., Xiao, S., Ding, L., Narasimhan, A., Chen, X., Wang, W., Li, Y., Elowsky, C., et al. (2025). Confocal Airy beam oblique light-sheet tomography for brain-wide cell type distribution and morphology. Nat. Methods *22*, 2622–2630. https://doi.org/10.1038/s41592-025-02888-9.

64. Steward, O., Wallace, C.S., Lyford, G.L., and Worley, P.F. (1998). Synaptic Activation Causes the mRNA for the IEG Arc to Localize Selectively near Activated Postsynaptic Sites on Dendrites. Neuron *21*, 741–751. https://doi.org/10.1016/S0896-6273(00)80591-7.

65. Hacisuleyman, E., Hale, C.R., Noble, N., Luo, J.D., Fak, J.J., Saito, M., Chen, J., Weissman, J.S., and Darnell, R.B. (2024). Neuronal activity rapidly reprograms dendritic translation via eIF4G2:uORF binding. Nat. Neurosci. *27*, 822–835. https://doi.org/10.1038/s41593-024-01615-5.

66. Poulopoulos, A., Murphy, A.J., Ozkan, A., Davis, P., Hatch, J., Kirchner, R., and Macklis, J.D. (2019). Subcellular transcriptomes and proteomes of developing axon projections in the cerebral cortex. Nature *565*, 356–360. https://doi.org/10.1038/s41586-018-0847-y.

67. Veeraraghavan, P., Engmann, A.K., Hatch, J.J., Itoh, Y., Nguyen, D., Addison, T., and Macklis, J.D. (2026). Dynamic subtype- and context-specific subcellular RNA regulation in growth cones of developing neurons of the cerebral cortex. Nat. Neurosci. *29*, 581–591. https://doi.org/10.1038/s41593-025-02173-0.

68. Goltstein, P.M., Reinert, S., Bonhoeffer, T., and Hübener, M. (2021). Mouse visual cortex areas represent perceptual and semantic features of learned visual categories. Nat. Neurosci. *24*, 1441–1451. https://doi.org/10.1038/s41593-021-00914-5.

69. Li, Y.T., Turan, Z., and Meister, M. (2020). Functional Architecture of Motion Direction in the Mouse Superior Colliculus. Curr. Biol. *30*, 3304–3315. https://doi.org/10.1016/j.cub.2020.06.023.

70. Xiong, F., Liu, L., and Peng, H. (2025). Reconstruction of a connectome of single neurons in mouse brains by cross-validating multi-scale multi-modality data. Nat. Methods *22*, 2670–2683. https://doi.org/10.1038/s41592-025-02784-2.

71. Fang, R., Halpern, A.R., Rahman, M.M., Huang, Z., Lei, Z., Hell, S.J., Dulac, C., and Zhuang, X. (2024). Three-dimensional single-cell transcriptome imaging of thick tissues. eLife *12*, RP90029. https://doi.org/10.7554/eLife.90029.

72. Sui, X., Lo, J.A., Luo, S., He, Y., Tang, Z., Lin, Z., Barabási, D.L., Zhou, Y., Wang, W.X., Liu, J., et al. (2025). Scalable spatial single-cell transcriptomics and translatomics in 3D thick tissue blocks. Nat. Methods *22*, 2574–2584. https://doi.org/10.1038/s41592-025-02867-0.

73. Nathanson, J.L., Yanagawa, Y., Obata, K., and Callaway, E.M. (2009). Preferential labeling of inhibitory and excitatory cortical neurons by endogenous tropism of adeno-associated virus and lentivirus vectors. Neuroscience *161*, 441–450. https://doi.org/10.1016/j.neuroscience.2009.03.032.

74. Pachitariu, M., Stringer, C., Dipoppa, M., Schröder, S., Rossi, L.F., Dalgleish, H., Carandini, M., and Harris, K.D. (2017). Suite2p: beyond 10,000 neurons with standard two-photon microscopy. Preprint at bioRxiv. https://doi.org/10.1101/061507.

75. Stringer, C., and Pachitariu, M. (2025). Cellpose3: one-click image restoration for improved cellular segmentation. Nat. Methods *22*, 592–599. https://doi.org/10.1038/s41592-025-02595-5.

76. Pachitariu, M., Rariden, M., and Stringer, C. (2025). Cellpose-SAM: superhuman generalization for cellular segmentation. Preprint at bioRxiv. https://doi.org/10.1101/2025.04.28.651001.

77. Lionnet, T., Czaplinski, K., Darzacq, X., Shav-Tal, Y., Wells, A.L., Chao, J.A., Park, H.Y., de Turris, V., Lopez-Jones, M., and Singer, R.H. (2011). A transgenic mouse for in vivo detection of endogenous labeled mRNA. Nat. Methods *8*, 165–170. https://doi.org/10.1038/nmeth.1551.

78. Bai, L., Cong, L., Shi, Z., Zhao, Y., Zhang, Y., Lu, B., Zhang, J., Xiong, Z.-Q., Xu, N., Mu, Y., et al. (2024). Volumetric voltage imaging of neuronal populations in the mouse brain by confocal light-field microscopy. Nat. Methods *21*, 2160–2170. https://doi.org/10.1038/s41592-024-02458-5.

79. Juavinett, A.L., Nauhaus, I., Garrett, M.E., Zhuang, J., and Callaway, E.M. (2017). Automated identification of mouse visual areas with intrinsic signal imaging. Nat. Protoc. *12*, 32–43. https://doi.org/10.1038/nprot.2016.158.

80. Garrett, M.E., Nauhaus, I., Marshel, J.H., and Callaway, E.M. (2014). Topography and Areal Organization of Mouse Visual Cortex. J. Neurosci. *34*, 12587–12600. https://doi.org/10.1523/JNEUROSCI.1124-14.2014.

81. Friedrich, J., Zhou, P., and Paninski, L. (2017). Fast online deconvolution of calcium imaging data. PLoS Comput. Biol. *13*, e1005423. https://doi.org/10.1371/journal.pcbi.1005423.

82. Choi, H.M.T., Schwarzkopf, M., Fornace, M.E., Acharya, A., Artavanis, G., Stegmaier, J., Cunha, A., and Pierce, N.A. (2018). Third-generation in situ hybridization chain reaction: multiplexed, quantitative, sensitive, versatile, robust. Development *145*, dev165753. https://doi.org/10.1242/dev.165753.

83. Schwarzkopf, M., Liu, M.C., Schulte, S.J., Ives, R., Husain, N., Choi, H.M.T., and Pierce, N.A. (2021). Hybridization chain reaction enables a unified approach to multiplexed, quantitative, high-resolution immunohistochemistry and in situ hybridization. Development *148*, dev199847. https://doi.org/10.1242/dev.199847.

84. Cock, P.J.A., Antao, T., Chang, J.T., Chapman, B.A., Cox, C.J., Dalke, A., Friedberg, I., Hamelryck, T., Kauff, F., Wilczynski, B., et al. (2009). Biopython: freely available Python tools for computational molecular biology and bioinformatics. Bioinformatics *25*, 1422–1423. https://doi.org/10.1093/bioinformatics/btp163.

85. Qiu, S., Hu, Y., Huang, Y., Gao, T., Wang, X., Wang, D., Ren, B., Shi, X., Chen, Y., Wang, X., et al. (2024). Whole-brain spatial organization of hippocampal single-neuron projectomes. Science *383*, eadj9198. https://doi.org/10.1126/science.adj9198.

86. Avants, B.B., Epstein, C.L., Grossman, M., and Gee, J.C. (2008). Symmetric diffeomorphic image registration with cross-correlation: Evaluating automated labeling of elderly and neurodegenerative brain. Med. Image Anal. *12*, 26–41. https://doi.org/10.1016/j.media.2007.06.004.

87. Stringer, C., Pachitariu, M., Steinmetz, N., Reddy, C.B., Carandini, M., and Harris, K.D. (2019). Spontaneous behaviors drive multidimensional, brainwide activity. Science *364*, eaav7893. https://doi.org/10.1126/science.aav7893.

88. Engelhard, B., Finkelstein, J., Cox, J., Fleming, W., Jang, H.J., Ornelas, S., Koay, S.A., Thiberge, S.Y., Daw, N.D., Tank, D.W., et al. (2019). Specialized coding of sensory, motor and cognitive variables in VTA dopamine neurons. Nature *570*, 509–513. https://doi.org/10.1038/s41586-019-1261-9.

89. Tustison, N.J., Cook, P.A., Holbrook, A.J., Johnson, H.J., Muschelli, J., Devenyi, G.A., Duda, J.T., Das, S.R., Cullen, N.C., Gillen, D.L., et al. (2021). The ANTsX ecosystem for quantitative biological and medical imaging. Sci. Rep. *11*, 9068. https://doi.org/10.1038/s41598-021-87564-6.

90. Hao, Y., Stuart, T., Kowalski, M.H., Choudhary, S., Hoffman, P., Hartman, A., Srivastava, A., Molla, G., Madad, S., Fernandez-Granda, C., et al. (2024). Dictionary learning for integrative, multimodal and scalable single-cell analysis. Nat. Biotechnol. *42*, 293–304. https://doi.org/10.1038/s41587-023-01767-y.

91. Stringer, C., Wang, T., Michaelos, M., and Pachitariu, M. (2021). Cellpose: a generalist algorithm for cellular segmentation. Nat. Methods *18*, 100–106. https://doi.org/10.1038/s41592-020-01018-x.

92. Schmidt, U., Weigert, M., Broaddus, C., and Myers, G. (2018). Cell Detection with Star-Convex Polygons. In Medical Image Computing and Computer Assisted Intervention – MICCAI 2018, A.F. Frangi, J.A. Schnabel, C. Davatzikos, C. Alberola-López, and G. Fichtinger, eds. (Springer International Publishing), pp. 265–273. https://doi.org/10.1007/978-3-030-00934-2_30.

93. Weigert, M., Schmidt, U., Haase, R., Sugawara, K., and Myers, G. (2020). Star-convex Polyhedra for 3D Object Detection and Segmentation in Microscopy. In IEEE Winter Conference on Applications of Computer Vision (WACV), pp. 3655–3662. https://doi.org/10.1109/WACV45572.2020.9093435.

94. Wolf, F.A., Angerer, P., and Theis, F.J. (2018). SCANPY: large-scale single-cell gene expression data analysis. Genome Biol. *19*, 15. https://doi.org/10.1186/s13059-017-1382-0.

Please cite this article in press as: Zhao et al., Multimodal imaging of gene expression, morphology, and activity of the same neuron, Cell (2026), https://doi.org/10.1016/j.cell.2026.05.041

CellPress

STAR★METHODS

KEY RESOURCES TABLE

REAGENT or RESOURCE	SOURCE	IDENTIFIER
Bacterial and virus strains		
pAAV2/8-EF1a-DIO-EYFP-WPRE-HGHpA	Taitool	Cat#S0196-8
pAAV2/9-hSyn-DIO-mEGFP-WPRE-pA	Taitool	Cat#S0276-9
pAAV2/9-hSyn-FLEX-GCaMP6s-WPRE-pA	Taitool	Cat#S0226-9
pAAV2/9-hSyn-FLEX-jGCaMP8m-WPRE-pA	Taitool	Cat#S1124-9
pAAV2/9-mCaMKIIa-iCre-WPRE-pA	Taitool	Cat#S0906-9
pAAV2/8-hSyn-DIO-EGFP-WPRE-pA	Taitool	Cat#S0746-8
pAAV2/9-hSyn-Cre-WPRE-pA	Taitool	Cat#S0278-9
Chemicals, peptides, and recombinant proteins		
PBS (pH 7.3, DNase, RNase & Protease free, Sterile)	Beyotime	Cat#ST477
PFA (4%, RNase free)	Bioss	Cat#C2055
Tert-butanol	Sigma	Cat#19460
Benzyl alcohol	Sigma	Cat#305197
Benzyl benzoate	Sigma	Cat#B6630
Trimethylamine	Sigma	Cat#90340
Quadrol	Sigma	Cat#122262
Vetbond	3M	CAS:6606-65-1
Isoflurane	VetOne	NDC:13985-030-60
Sylgard 184	Sigma	Cat#761028-5EA
MOPS	Sigma	Cat#M1254
Melphalan	Cayman Chemical	Cat#16665
Acryloyl-X, SE	Thermo Fisher	Cat#A20770
Anhydrous DMSO	Invitrogen	Cat#D12345
Acrylic acid	Sigma	Cat#147230-500G
Acrylamide solution (40%)	Sigma	Cat#A4058-100ML
N, N'-Methylenebisacrylamide	Sigma	Cat#M7279-25G
NaCl (5 M), RNase free	Invitrogen	Cat#AM9759
4-Hydroxy-TEMPO	Sigma	Cat#176141
N,N,N′,N′-Tetramethylethylenediamine	Sigma	Cat#T7024
Ammonium persulfate	Sigma	Cat#A3678
Proteinase K	NEB	Cat#P8107S
Tris (1 M), pH 8.0, RNase free	Invitrogen	Cat#AM9856
Triton X-100	Sigma	Cat#T8787-100ML
EDTA (0.5 M), pH 8.0, RNase free	Invitrogen	Cat#AM9261
SDS, 10% solution, RNase free	Invitrogen	Cat#AM9822
MgCl2 (1 M), RNase free	Invitrogen	Cat#AM9530G
CaCl2 (1 M), RNase free	Sigma	Cat#21115-100ML
RNase-free DNase Set (50)	Qiagen	Cat#79254
Poly-lysine solution (0.1% (w/v))	Sigma	Cat#P8920-100ML
Nuclease-free Water	Qiagen	Cat#129115
10 × PBS, pH 7.4, RNase free	Invitrogen	Cat#AM9625
TWEEN 20	Sigma	Cat#P7949-100ML

(*Continued on next page*)

Please cite this article in press as: Zhao et al., Multimodal imaging of gene expression, morphology, and activity of the same neuron, Cell (2026), https://doi.org/10.1016/j.cell.2026.05.041

Continued

REAGENT or RESOURCE	SOURCE	IDENTIFIER
20 × SSC, RNase free	Invitrogen	Cat#AM9763
DAPI	Sigma	Cat#D9542-5MG
RNase-away	Thermo Fisher	Cat#7002
Photo-Flo 200	Kodak	Cat#1026269
Janelia Fluor 669, SE	Tocris	Cat#6420
NaOH (10 M), RNase free	Sigma	Cat#72068-100ML
Deposited data		
Multimodal data	This paper	Brain Science Data Center, Chinese Academy of Sciences: https://doi.org/10.12412/BSDC.1760411296.20002
Custom codes for data acquisition and analysis	This paper	GitHub: https://github.com/WKLabION/Trimodal-Data-and-Analysis
Custom codes for data analysis	This paper	GitHub: https://github.com/WKLabION/Trimodal-Data-and-Analysis
Experimental models: Organisms/strains		
Mouse: C57BL/6J mice	JAX Laboratory	JAX:000664
Mouse: C57BL/6J-Tg(Thy1-GCaMP6s)GP4.3Dkim/J	JAX Laboratory	JAX:024275
Mouse: B6.FVB(Cg)-Tg(Rbp4-cre)KL100Gsat/Mmucd	MMRRC	RRID:MMRRC_037128-UCD
Oligonucleotides		
Cux2-I1(R1)	Tsingke BioTech	SHP24041600007
Satb2-I2(R1)	Tsingke BioTech	SHP22092500002
Eef2-I3(R1)	Tsingke BioTech	SHP23083000003
Vglut1-I4(R1)	Tsingke BioTech	SHP23071600005
Fezf2-I5(R1)	Molecular Instruments	N/A
Gad1-I6(R1)	Tsingke BioTech	SHP23080900019
Rspo1-I1(R2)	Tsingke BioTech	SHP24072400005
Col6a1-I2(R2)	Molecular Instruments	N/A
Slc30a3-I3(R2)	Tsingke BioTech	SHP23071600004
Sulf2-I4(R2)	Tsingke BioTech	SHP24071200011
Rprm-I5(R2)	Molecular Instruments	N/A
Rorb-I6(R2)	Tsingke BioTech	SHP23071600003
C1ql3-I1(R3)	Tsingke BioTech	SHP24072800002
Rbp4-I2(R3)	Molecular Instruments	N/A
Lmo4-I3(R3)	Tsingke BioTech	TSP20221205-021-00549
Bcl6-I4(R3)	Tsingke BioTech	SHP24072400004
Pvalb-I5(R3)	Molecular Instruments	N/A
Syt6-I6(R3)	Tsingke BioTech	SHP24072400006
Tshz2-I1(R4)	Tsingke BioTech	SHP24072800006
Dkk3-I2(R4)	Tsingke BioTech	TSP20221205-021-00547
Penk-I3(R4)	Molecular Instruments	N/A
Tbr1-I4(R4)	Tsingke BioTech	SHP24072400007
Tac1-I5(R4)	Molecular Instruments	N/A
Bcl11b-I6(R4)	Tsingke BioTech	SHP24072800001
Otof-I1(R5)	Sangon BioTech	112879377
Vip-I2(R5)	Molecular Instruments	N/A
Cdh9-I3(R5)	Tsingke BioTech	SHP23062900002

(*Continued on next page*)

Please cite this article in press as: Zhao et al., Multimodal imaging of gene expression, morphology, and activity of the same neuron, Cell (2026), https://doi.org/10.1016/j.cell.2026.05.041

Continued

REAGENT or RESOURCE	SOURCE	IDENTIFIER
Rasgrf2-I4(R5)	Tsingke BioTech	SHP24072800004
Cck-I5(R5)	Molecular Instruments	N/A
Etv1-I6(R5)	Tsingke BioTech	SHP24072800003
mEGFP-I1	Tsingke BioTech	SHP24060600002
I1-H1-Alexa Fluor488	Sangon BioTech	Order No. 112875004; Lot No. 1943490462
I1-H2-Alexa Fluor488	Sangon BioTech	Order No. 112875004; Lot No. 1943490463
I2-H1-Alexa Fluor546	Sangon BioTech	Order No. 113026773; Lot No. 1945138950
I2-H2-Alexa Fluor546	Sangon BioTech	Order No. 113026773; Lot No. 1945138949
I3-H1-Janelia Fluor669	Sangon BioTech	Order No. 112801537; Lot No. 1942701640
I3-H2-Janelia Fluor669	Sangon BioTech	Order No. 112801537; Lot No. 1942701641
I4-H1-Alexa Fluor488	Sangon BioTech	Order No. 112875004; Lot No. 1943490461
I4-H2-Alexa Fluor546	Sangon BioTech	Order No. 112755498; Lot No. 1942233195
I5-H1-Alexa Fluor488	Sangon BioTech	Order No. 112875004; Lot No. 1943490459
I5-H2-Janelia Fluor669	Sangon BioTech	Order No. 112801537; Lot No. 1942701642
I6-H1-Alexa Fluor546	Sangon BioTech	Order No. 112878465; Lot No. 1943522900
I6-H2-Janelia Fluor669	Sangon BioTech	Order No. 112878465; Lot No. 1943522901
Software and algorithms		
ImageJ	Open Source	https://ImageJ.net/ImageJ
MATLAB	MathWorks	https://www.mathworks.com/products/matlab.html
Suite2p	Pachitariu et al.[74]	RRID: SCR_016434
Psychtoolbox	Psychophysics Toolbox	RRID: SCR_002881
LabVIEW	National Instruments	RRID: SCR_014325
Cellpose v3.0	Pachitariu and Stringer.[75]	https://github.com/MouseLand/cellpose
Cellpose-SAM	Pachitariu et al.[76]	https://github.com/MouseLand/cellpose
AIRLOCALIZE	Lionnet et al.[77]	https://github.com/timotheelionnet/AIRLOCALIZE/
ANTs	V2.4.4	https://github.com/ANTsX/ANTs
R	V4.5.0	https://cran.r-project.org/
Seurat	V5.3.0	https://satijalab.org/seurat/
ComplexHeatmap	V2.21.1	https://github.com/jokergoo/ComplexHeatmap
Python	V3.13.2	https://www.python.org/
SankeyMATIC		https://sankeymatic.com/
Scanpy	V1.11.1	https://github.com/scverse/scanpy
BLAST+	2.13.0	https://blast.ncbi.nlm.nih.gov/Blast.cgi
Biopython	1.81	https://biopython.org/
NUPACK	4.0.1.12	https://nupack.org/
Other		
Zeiss Lightsheet 7 microscope	Zeiss	https://www.zeiss.com/microscopy/en/products/light-microscopes/light-sheet-microscopes/lightsheet-7.html
Slide	Citotest	Cat#80312-2201
Coverslip	Citotest	Cat#80340-3610
Press-to-Seal silicone isolators	Invitrogen	Cat#P24743
Laser 920	Spark	ALCOR 920-4
Mitutoyo M Plan NIR-HR 50× Objective	Edmund Optics	Cat#56-982
Holographic beam splitter	LBTEK	N/A
Galvo	Sino-galvo	Cat#SG7210

Please cite this article in press as: Zhao et al., Multimodal imaging of gene expression, morphology, and activity of the same neuron, Cell (2026), https://doi.org/10.1016/j.cell.2026.05.041

EXPERIMENTAL MODEL AND STUDY PARTICIPANT DETAILS

Animals

Adult male C57BL/6J mice (8–12 weeks old; Shanghai SLAC Laboratory Animal Co., Ltd.), Rbp4-Cre mice (strain B6.FVB(Cg)-Tg(Rbp4-cre)KL100Gsat/Mmucd; MMRRC) and Thy1-GCaMP6s mice (strain GP4.3Dkim/J; Jackson Laboratory) were used in this study. Mice were housed in individually ventilated cages under controlled temperature (21–23 °C) and humidity (40-70%), with a 12-h light/12-h dark cycle (lights on from 7:00 to 19:00). All imaging experiments were performed during the light phase. All experimental procedures were approved by the Animal Care and Use Committee of the Center for Excellence in Brain Science and Intelligence Technology, Chinese Academy of Sciences.

METHOD DETAILS

Mice preparation

For surgeries, mice were anesthetized with isoflurane (4% for induction; 1-1.5% for maintenance) and placed into a stereotaxic apparatus. Eyes were protected with erythromycin ophthalmic ointment to prevent drying and glare. After scalp removal, the skull surface was cleaned with sterile saline and a craniotomy (~3.0-3.5 mm diameter) was performed above the primary visual cortex (VISp; anterior-posterior: -3.8 mm; medial-lateral: -2.6 mm from Bregma) using a high-speed drill with continuous saline irrigation to minimize heating. Viral injections were performed using a microinjection system (WPI, Micro4). For whole-brain structural imaging, AAV2/9-hSyn-Cre-WPRE-pA and AAV2/9-hSyn-FLEX-EGFP-WPRE-pA (Taitool BioScience) were injected. For two-photon functional imaging, either AAV2/9-mCaMKIIa-iCre-WPRE-pA or AAV2/9-hSyn-Cre-WPRE-pA was co-injected with AAV2/9-hSyn-FLEX-GCaMP6s-WPRE-pA or AAV2/9-hSyn-FLEX-jGCaMP8m-WPRE-pA (Table S1). After injections, a cranial window and a custom-designed titanium headpost were attached to the skull using cyanoacrylate glue (Loctite 495) and then reinforced with dental acrylic. Two types of cranial windows were used depending on the imaging modality. For functional imaging alone, as shown in Figure 7, a fixed glass window was implanted. The glass window consisted of two layers: a 5-mm diameter, 0.17-mm thick circular coverslip bonded concentrically to a 3-mm diameter, 0.4-mm thick circular coverslip using ultraviolet-curing adhesive. For multimodal imaging in the IMC platform, a flexible polydimethylsiloxane (PDMS) window was implanted.[78] Following surgery, mice recovered for at least 2 weeks, and imaging was performed no earlier than 4 weeks post-viral injection to ensure stable GCaMP expression. Prior to imaging, animals were head-fixed on a customized holder and habituated daily for 15–30 min. During imaging sessions, mice were kept awake, head-fixed, and allowed to rest quietly on a platform.

Flexible window preparation and second injection

The flexible window was constructed by attaching a thin PDMS film (Sylgard, 184 Silicone Elastomer Kit) to a glass slide ring. The PDMS film was prepared by thoroughly mixing the elastomer base and curing agent in a 10:1 ratio, spreading the mixture on a glass plate and degassing in a vacuum desiccator (−0.1 MPa, Titan, VD-R6). A thickness of 0.4 mm was chosen for the film to allow high-quality imaging. After degassing, the liquid PDMS was covered with another glass plate to ensure uniform thickness of the film. After curing at 80 °C for 2 h, the PDMS film was peeled off and cut into circular pieces with a diameter of 3.5 mm. The circular PDMS pieces were then bonded to customized glass slide rings (thickness of 150 μm, outer diameter of 5 mm, inner diameter of 2.5 mm) by treating their bonding surfaces with plasma (Relyon plasma, PiezoBrush PZ3) for 5 s and baking at 90 °C for 4 h. The prepared PDMS windows were sterilized with ultraviolet light and stored in a dust-free petri dish ready for use. A second viral injection was performed to enhance morphological labeling after functional imaging. The second injection was conducted 1–3 days following functional imaging through the existing PDMS window. Anesthesia and animal preparation followed the same procedures as in mouse surgery, with isoflurane maintained at 1% during the injection. For secondary labeling, AAV2/9-hSyn-DIO-mEGFP-WPRE-pA (titer: 2.9×10^{12} vg/mL, Taitool Bioscience) was injected near the previously imaged neurons. Injections were targeted to locations 300–400 μm lateral to the functionally imaged neurons at depths corresponding to the original imaging plane. 2-3 injection sites were used to cover the imaged region, with 200 nL delivered at each site over 5–10 min. Following the second injection, mice were allowed to recover for two weeks to ensure sufficient viral expression prior to subsequent structural imaging of the same neurons.

Intrinsic signal optical imaging

During intrinsic signal optical imaging, mice were maintained under light anesthesia (1% isoflurane) with head fixation. A white light source (Thorlabs, SLS201L/M), filtered through an optical bandpass filter (Edmund, 86-953, 625/50), was used to perform bright-field imaging on the mouse brain.[79] Visual stimuli (drifting bar stimuli with black-white checkerboard patterns) were presented in four cardinal directions (0°, 90°, 180°, 270°), with 10 repetitions per direction, using a 17-inch monitor positioned ~12 cm from the mouse's left eye. The monitor was rotated ~30° in the coronal plane and tilted ~70° from horizontal to achieve perpendicular alignment with the visual axis. Prior to imaging, the focal plane was positioned 300-500 μm below the cortical surface to minimize vascular artifacts. Data acquisition required ≥10 stimulus trials to ensure sufficient signal-to-noise ratio for detecting stimulus-evoked activity. Retinotopic analysis was performed as follows: (1) Horizontal and vertical retinotopic maps were generated from temporal phase responses to drifting bars. (2) Maps were smoothed using a 2D Gaussian kernel ($\sigma = 25$ μm). (3) Visual field sign maps were computed as the sine of the difference between the vertical and horizontal retinotopic gradients at each pixel. (4) Area boundaries were identified at

Please cite this article in press as: Zhao et al., Multimodal imaging of gene expression, morphology, and activity of the same neuron, Cell (2026), https://doi.org/10.1016/j.cell.2026.05.041

retinotopic gradient reversals in field sign maps.[80] Manually delineated boundaries enabled visual field map reconstruction, with bright-field vasculature patterns providing alignment landmarks for subsequent two-photon imaging experiments.

Visual stimulation

Visual stimuli were presented on an LCD monitor (Dell E1715S; 1280 × 1024 resolution, 60 Hz refresh rate) positioned ~12 cm from the mouse's left eye and centered on the visual field. Stimuli included: Drifting gratings: Sinusoidal patterns (80% contrast, 0.8 Hz temporal frequency, 0.04 cycles per degree) moving in four directions (0°, 90°, 180°, 270°). Checkerboard stimuli: Stationary counter-phase-alternating gratings (0.04 cycles per degree in both x and y directions, 2 Hz reversal frequency). Stimulus delivery was controlled via MATLAB Psychophysics Toolbox. Presentation parameters: (1) 2 s stimulus duration. (2) 4-6 s interstimulus interval (uniform gray screen). (3) 10 trials per condition. (4) Pseudo-randomized trial sequence.

Two-photon functional imaging

Imaging was performed with a two-photon microscope 8 weeks after viral injection. Mice were head-fixed and awake during the imaging session. Before imaging, mice were habituated to the imaging setup for at least 1 h. One complete imaging session lasted about 6 min. Inter-session intervals were set as 10 min. Multiple imaging sessions were performed on the same mouse for distinct depths and FOVs, but on different days. Images were acquired at 15 Hz, 1024 × 1024 pixels (800 x 800 μm) or 30 Hz, 512 × 512 pixels (400 x 400 μm). The imaging depths (~200 μm-550 μm) were identified by the distance relative to the dura surface. Per-session recordings consisted of 5,600 frames (15 Hz) or 11,200 frames (30 Hz). Motion artifacts were corrected using rigid-body cross-correlation registration (MATLAB R2021b). Following registration: (1) Somatic regions were manually segmented. (2) ROI fluorescence was background-subtracted. (3) Baseline fluorescence (F_0) was derived via custom deconvolution,[81] which was utilized for subsequent analysis.

Tissue clearing and rehydration

All solutions were prepared using RNase-free reagents. Following perfusion, the mouse brain was post-fixed in 4% paraformaldehyde (PFA) for 24 hours at 4°C and then thoroughly rinsed with ice-cold phosphate-buffered saline (PBS; three times). For dehydration, the intact brain was sequentially incubated in a graded series of tert-butanol solutions (30%, 50%, 70%, 80%, 96%, 100%, 100%) for 24 hours per concentration. The graded tert-butanol solutions were prepared by mixing tert-butanol with distilled water at the following volume/volume (v/v) ratios: 30%, 50%, 70%, 80%, 96%, and 100%. Quadrol (3% w/v) was added for pH adjustment. This clearing procedure removed lipids, but mEGFP remained intact, as it was anchored to an insoluble protein scaffold in fixation prior to clearing. After dehydration, the brain was transferred to Benzyl Alcohol-Benzyl Benzoate (BABB) solution for 2 days to achieve delipidation and clearing. The BABB solution was prepared by mixing benzyl alcohol and benzyl benzoate at a 1:2 volume ratio. Quadrol (3% w/v per 9 mL of the mixture) was also added for pH adjustment. Rehydration was performed as the reverse procedure: the cleared brain was sequentially incubated in a decreasing concentration series of tert-butanol solutions (100%, 100%, 96%, 80%, 70%, 50%, 30%) for 24 hours per concentration (Figure S2B), and was finally transferred back to PBS for subsequent sectioning and the 2cEASI-FISH experiment. All procedures were conducted protected from light with continuous agitation on a temperature-controlled orbital shaker maintained at 30.0 ± 0.5°C and 80 rpm.

Multi-plane two-photon imaging system

The optical system is detailed in Figure S2C. In the excitation light path, a 920 nm femtosecond laser (ALCOR 920-4) beam was power-controlled using a half-wave plate (Daheng Optics, GCL-060812) and a polarizing beam splitter (LBTEK, MPBS643). The beam was expanded to a diameter of 15 mm using a pair of achromatic lenses L1 (Edmund, 49-352, f = 30 mm) and L2 (Edmund, 49-365, f = 225 mm), and then directed onto a customized holographic beam splitter (LBTEK, beam-splitting DOE). The diffracted laser beam was focused into eight spots distributed in 3D by a compound lens L3, which consists of a pair of achromatic lenses (LBTEK, AD524-B, f = 500 mm & AD529-B, f = 1000 mm). A customized spatial filter was placed at the focal plane of L3 to selectively pass the first-order diffracted beams and one high-order diffracted beam, which was used to monitor the scanning angle of the galvo. The filtered multi-focal beam was relayed to the sample plane by two pairs of lenses that were all arranged in 4-f configurations, including L4 (Edmund, 49-361, f = 125 mm) & L5 (Edmund, 49-391, f = 150 mm) and L6 (Edmund, 49-391, f = 150 mm) & Objective (Mitutoyo, M Plan NIR-HR50×, NA 0.65). A pair of galvo scanners (Sino-Galvo (Jiangsu) Technology Co.) was placed between L4 and L5, conjugated to the back pupil of the objective. A customized glass dome (Changchun Bright Photoelectric Technology Co., Dia = 14 mm, R1 = 9 mm, R2 = 11 mm) was sealed to a sample chamber and positioned above the imaging objective. The center of the glass dome was aligned to the objective's focal plane, allowing the converging spherical wavefront of the excitation laser to focus into the high-RI medium with minimal wavefront distortion. During imaging, the sample was held by a customized holder and scanned in 3D using a combination of scanning stages (Newport, ONE-XY60 for x-y plane and Physik Instrumente (PI), Q545.240 for z-direction). The fluorescent signal was collected by the imaging objective, de-scanned by the galvo scanner and then directed away from the excitation light path by a dichroic mirror DM (Semrock, FF875-Di01). It was filtered through an optical filter F (Semrock, FF01-680/SP and FF01-520/70) and focused into eight spots by a compound lens L7 consisting of two achromatic lenses (Thorlabs, AC254-250-A, f = 250 mm & AC254-200-A, f = 200 mm). The spacing between these two lenses was adjusted to precisely direct fluorescent signals from eight different excitation focal spots into eight multimode fibers (Thorlabs, FG550UEC, NA = 0.22). Eight

Please cite this article in press as: Zhao et al., Multimodal imaging of gene expression, morphology, and activity of the same neuron, Cell (2026), https://doi.org/10.1016/j.cell.2026.05.041

photodetectors (Hamamatsu, C13366-3050GA) were connected to the multimode fibers for simultaneous signal detection. The analog signals from the detectors were low-pass filtered (Zhongshan Feierte Communication Equipment Co., LPF-200 kHz) and digitized (NI, PXIE-5105) for image reconstruction. In addition, the signal from a photodetector (Thorlabs, PDA36A-EC) that monitors the galvo scanning using the high-order diffracted laser beam was also digitized to facilitate image reconstruction with high precision. Hardware control and data acquisition were achieved through a LabVIEW (2015) program. We implemented two scanning modes: stage scan and galvo scan. In stage scan mode, x-y scanning was achieved using the x-galvo and y-stage, allowing for large FOV whole-brain imaging. In galvo scan mode, scanning in the y-direction was performed using the y-galvo instead of the y-stage, facilitating more precise measurement of the PSFs (Figures 3C and S2F) and more detailed morphological characterization (Figure 3D).

Tissue fixation and preparation

C57BL/6J mice after *in vivo* two-photon imaging were used for whole-brain projection imaging and all further FISH detection experiments. Animals were anesthetized with isoflurane and perfused with RNase-free PBS followed by ice-cold 4% paraformaldehyde (PFA). After whole mouse brain clearing for projection imaging, brains were rehydrated and stored in RNase-free 1 × PBS for subsequent FISH experiments. Brain coronal slices (200 μm) were sectioned and stored in RNase-free 1 × PBS. Slices containing mEGFP labeled neurons were selected and imaged under fluorescence microscope. Brain regions containing mEGFP-labeled neurons were cut into ∼2 × 1 mm rectangles for easier optimal orientation imaging. All brushes and equipment used were treated with RNase Away to prevent RNA degradation.

Design and synthesis of six dual-color orthogonal HCR systems

Each orthogonal hybridization chain reaction (HCR) system consisted of a pair of hairpins and a corresponding initiator. Hairpins were 72 nucleotides in length and designed with a 12-nt toehold, 24-nt stem, and 12-nt loop region. Systems I1 through I5 were adopted from previously validated designs in HCR v3.0.[82] System I6 was designed de novo using NUPACK software to thermodynamically optimize nucleic acid hybridization, following the principles previously described.[83] Each hairpin pair was labeled with specific fluorophores to enable dual-color detection. The fluorophore assignments were as follows (Figure 5A):

System I1: Hairpin 1 and hairpin 2 labeled with Alexa Fluor 488;
System I2: Hairpin 1 and hairpin 2 labeled with Alexa Fluor 546;
System I3: Hairpin 1 and hairpin 2 labeled with Janelia Fluor 669;
System I4: Hairpin 1 labeled with Alexa Fluor 488; hairpin 2 with Alexa Fluor 546;
System I5: Hairpin 1 labeled with Alexa Fluor 488; hairpin 2 with Janelia Fluor 669;
System I6: Hairpin 1 labeled with Alexa Fluor 546; hairpin 2 with Janelia Fluor 669.

All oligonucleotides were synthesized, fluorophore-conjugated, and HPLC-purified by Sangon Biotech (Shanghai, China). See key resources table for detailed reagent information.

Orthogonal validation of the HCR system

All hairpins were snap-cooled in a PCR thermocycler (95 °C for 5 min then cooled at room temperature for 30 min). HCR reactions were performed in 20 μL volumes containing 150 nM of each hairpin and one of the following: (i) 30 nM of the corresponding cognate initiator, (ii) a mixture of all five non-cognate initiators (30 nM each, "Others"), or (iii) 5× SSC buffer as a negative control. Reactions were incubated at room temperature for 3 hours. To assess amplification and orthogonality, 18 μL of each reaction product was mixed with 2 μL of 5× loading buffer and loaded onto a 2% agarose gel. Electrophoresis was performed in 1× TAE buffer at 120 V for 35 minutes. A DL2000 Plus DNA ladder (Takara) served as the molecular weight marker. Gels were imaged using a UVP ChemStudio Imaging System (Analytik Jena, Germany). No cross-reactivity was observed between non-cognate initiator-hairpin pairs, confirming the orthogonality of the HCR design.

Design and synthesis of split-initiator HCR probes

Each mRNA probe was 45 nucleotides in length, comprising an 18-nt initiator sequence, a 2-nt spacer, and a 25-nt target recognition sequence. Pairs of adjacent probes (∼20 pairs per gene) were designed to hybridize next to each other on the target transcript and collectively assemble a functional initiator, thereby triggering downstream HCR amplification. Candidate recognition sequences (52 nt) were initially selected based on the following criteria: melting temperature < 80 °C, GC content between 40–60%, and absence of homopolymeric runs (> 4 consecutive identical nucleotides). To ensure probe specificity, these sequences were screened against the mouse reference transcriptome using local BLAST+ via the *Biopython* function "*NcbiblastnCommandline*"[84] (https://github.com/biopython/biopython). Qualified 52-nt sequences were then split into two 25-nt target recognition segments with 2-nt interval, and paired with an 18-nt split-initiator (I1-I6, based on color code) and a 2-nt spacer to generate the final probe designs. All custom probes were synthesized with HPLC purification by Tsingke Biotech (Shanghai, China) or Sangon Biotech (Shanghai, China). Additional probes were purchased from Molecular Instruments (Los Angeles, CA, USA). Full probe details are listed in key resources table.

Please cite this article in press as: Zhao et al., Multimodal imaging of gene expression, morphology, and activity of the same neuron, Cell (2026), https://doi.org/10.1016/j.cell.2026.05.041

CellPress

2cEASI-FISH imaging

To enable cross-modality alignment with functional and structural datasets, rehydrated mEGFP-labeled brains (See tissue clearing and rehydration) were sectioned into 200 μm thick slices. The thick slices were rehydrated in PBS at room temperature (2 × 10 min), followed by incubation in MOPS buffer for 30 minutes. Samples then underwent RNA anchoring, gelation, Proteinase K digestion, and DNase I treatment with minor modifications to a previously described protocol.[26] To align the mEGFP-labeled neurons in thick tissue with prior functional and structural images, mEGFP and cytosolic DAPI (cytoDAPI) signals were acquired at 10x magnification (20× objective, zoom 0.5×). To preserve the green channel for subsequent 2cEASI-FISH, the mEGFP signal was then photobleached using 405 nm laser at 4 mW and 100 ms exposure (Figure 5A). The cytoDAPI images were used for cell segmentation and registration across all 2cEASI-FISH rounds. Subsequently, 5 rounds of 2cEASI-FISH were performed to detect a total of 30 genes, based on a previously established EASI-FISH protocol with the modification of incorporating six orthogonal initiator–hairpin sets per round (Figures 5A and S7A), allowing simultaneous detection of six genes. In a subset of samples (34 neurons in the trimodal dataset), a sixth round of 2cEASI-FISH was performed to assess mRNA retention.

All 2cEASI-FISH imaging was conducted in PBS with 2 × expansion using a Zeiss Lightsheet 7 microscope. To resolve single mRNA molecules for dual-color hairpin decoding (See 2cEASI-FISH data processing), a 20x water-immersion objective (20x/1.0 W Plan-Apochromat Corr DIC M27 75 mm, RI = 1.33) was used for imaging with zoom 2.5× (final magnification 50×). Single-side illumination was used to minimize alignment errors. The four imaging channels were acquired sequentially using a single camera, with laser powers set as follows: 3.9 mW at 405 nm, 10.9 mW at 488 nm, 8.2 mW at 546 nm, and 27.4 mW at 669 nm. Images were acquired at 0.09 μm × 0.09 μm lateral resolution and 0.36 μm axial step size (post-expansion), with each tile covering 1920 × 1920 pixels (~86 μm × 86 μm, pre-expansion) and ~100 z-slices. The mean photon counts per pixel on bright spots representing individual labeled RNA molecules in different channels were 179 (488 nm), 170 (546 nm) and 109 (669 nm). Imaging was targeted to sparsely labeled neurons previously characterized in functional and structural experiments, significantly reducing data volume and processing time.

QUANTIFICATION AND STATISTICAL ANALYSIS

Single-cell neuron tracing and quality control

Each brain sample yielded approximately 6,000 raw 16-bit TIF image stacks, with each stack containing images simultaneously acquired from eight detection channels, corresponding to the eight multi-plane two-photon excitation foci. The raw stacks were first processed by performing channel registration to correct for spatial offsets between detectors. This was followed by image stitching to reconstruct the volumes of the two half-brains. The two volumes were then combined using 3D affine transformation based on common structural features in the overlapping regions (Figure S5A). The stitched 3D volume was then divided into 64,000 data cubes, each of size 360 × 400 × 80 voxels, to facilitate efficient manual reconstruction. Neuronal tracing was performed using Fast Neurite Tracer (FNT) software.[25] Each neuron was independently traced by two experienced annotators. The final consensus reconstruction for each neuron was subsequently generated by a third expert annotator.

Axonal reconstructions passed QC if axon length exceeded 10 mm (IT) or 20 mm (PT). To enhance model robustness and minimize overfitting from sparsely innervated targets, a brain region was retained if ≥20% of neurons had > 1 mm total axon in that region. For dendritic reconstructions, basal and apical arbors were quality-controlled separately (Figures S3A and S3B). High-quality dendrites were defined by the absence of incomplete neurites, the lack of abrupt terminations, and a high signal-to-noise ratio.

Whole brain registration

To register reconstructed neurons into the Allen Mouse Brain Common Coordinate Framework version 3 (CCFv3),[34] we performed a two-step registration procedure consisting of affine alignment followed by non-linear registration.[85] First, manual segmentation was performed on multiple anatomical landmarks to guide registration. These landmarks include: whole brain outline, hippocampus and subiculum (HIP-SUB), hypothalamus and thalamus outline (HY-TH), anterior commissure (olfactory and temporal limbs; aco-act), cerebral aqueduct and fourth ventricle (AQ-V4), caudate putamen (CP), dentate gyrus supragranular layer (DG-sg), corpus callosum and fasciculus (fa-ccg-ccb), fasciculus retroflexus (fr), fornix (fx), granular layer (gr), medial habenula (mh), mammillothalamic tract (mtt), optic chiasm (och), pontine gray (PG), paraventricular hypothalamic nucleus (PVH), facial nerve (VIIn), third ventricle (VL-V3), and isocortex (iso). Each structure was assigned an artificial intensity value to enhance feature contrast for registration: 128, 200, 170, 255, 180, 170, 60, 255, 255, 255, 230, 255, 255, 255, 255, 255, 60, 40, and 100, respectively. Following manual segmentation, initial global alignment was performed using affine transformation, followed by non-linear 3D registration using the ANTs (Advanced Normalization Tools) framework to refine local deformations.[86] The resulting transformation matrices were applied to the reconstructed neurons to map their coordinates into CCFv3 space. To evaluate registration accuracy, variability was assessed based on alignment of fasciculus retroflexus (fr), mammillothalamic tract (mtt), and cerebral aqueduct (AQ) across brain samples. The estimated registration precision was less than 20 μm (Figure S5B).

Please cite this article in press as: Zhao et al., Multimodal imaging of gene expression, morphology, and activity of the same neuron, Cell (2026), https://doi.org/10.1016/j.cell.2026.05.041

Projection-type classification

Projection classes were assigned based on registered whole-brain axonal reconstructions, following established conventions for cortical projection neuron classification.[24,35,36] Classification was determined solely from the spatial distribution of reconstructed long-range axonal arbors in the CCFv3. Neurons were categorized into the following projection classes:

Intratelencephalic (IT) neurons were defined as neurons whose reconstructed axonal arbors were confined to telencephalic structures, including ipsilateral and/or contralateral cerebral cortex and striatum. IT neurons exhibited no axonal segments extending into diencephalic, midbrain, or brainstem territories (i.e., no extratelencephalic targets). IT neurons were further subdivided into ipsilateral-IT and contralateral-IT subtypes based on the presence or absence of contralateral cortical arborization.

Pyramidal tract (PT) neurons were defined as neurons with axons extending beyond telencephalic structures into extratelencephalic regions. These included neurons exhibiting axonal projections to thalamic nuclei and/or midbrain or brainstem regions, consistent with pyramidal-tract–type output pathways.

Corticothalamic (CT) neurons were defined as neurons whose long-range axonal projections prominently innervated thalamic nuclei while remaining restricted to cortex, white matter, and thalamus, without descending midbrain or brainstem trajectories characteristic of PT neurons. CT neurons were not observed in the present dataset. This likely reflects the labeling and imaging strategy, including viral injection depth and the *in vivo* two-photon imaging depth range, which preferentially sampled superficial and layer 5 projection neurons.

Functional classification of neurons

To assign functional labels to individual neurons based on their visual and behavioral response profiles, we used a generalized linear model (GLM) framework to model the Ca^{2+} fluorescence trace ($\Delta F/F_0$) of each neuron. In GLM analysis, the design matrix included two categories of predictors: 1. Visual stimuli: Five stimulus conditions (checkerboard and drifting gratings in four directions). For each stimulus type, binary event vectors were constructed based on stimulus onset times. To capture stimulus-locked temporal dynamics, each event vector was convolved with a set of 7-degree-of-freedom B-spline basis functions spanning 3 seconds post-stimulus onset, yielding a set of time-varying stimulus kernels. 2. Facial movement: Facial movements were quantified as frame-to-frame image differences (motion energy).[87] Principal component analysis (PCA) was applied to extract the first principal component (PC1), which captured the dominant movement dynamics. The PC1 trace was z-scored and entered into the design matrix as two continuous regressors: motion energy (linear) and (motion energy)^2 (quadratic), allowing the model to capture both linear and nonlinear movement-related contributions.

For each neuron, the GLM yielded fitted response profiles to both stimulus and movement predictors. The significance of fitted response was assessed using a nested model comparison approach. Specifically, each response was tested by comparing the full model to a reduced model excluding the corresponding group of predictors. F-statistics were computed from the change in residual sum of squares (RSS) to quantify the reduction in explained variance.[88] Statistical significance was assessed by generating null distributions for the F-statistic via permutation testing. Ca^{2+} traces were randomly shuffled across 6,000 iterations using non-overlapping bins of randomized length (1-6 seconds) to preserve local temporal autocorrelation. Empirical p values were computed as the proportion of shuffled F-statistics exceeding the observed value. To account for multiple comparisons across the six predictors, Bonferroni correction was applied.

To ensure that functional categorization was not driven by isolated high-amplitude events, we incorporated an explicit trial-wise reliability criterion. Fluorescence traces were smoothed with a moving-average filter (3–5 points). For each trial, $\Delta F/F_0$ was computed using the 2 s pre-stimulus window as baseline. All baseline $\Delta F/F_0$ values across trials were pooled to form an empirical null distribution for that neuron. The stimulus-locked response window was defined as 0.5–2.5 s after stimulus onset. A trial was considered responsive if the maximum $\Delta F/F_0$ within this window exceeded the 95th percentile of the neuron's baseline distribution (one-sided). A neuron was classified as responsive to a given stimulus category only if it satisfied both (i) GLM significance (adjusted $p < 0.05$) and (ii) trial reliability (responsive in $\geq$50% of trials).

In some analyses, we categorized neurons into three groups: checkerboard-dominant, grating-dominant, or non-responsive, based on their responses to each type of visual stimulus. Checkerboard-dominant neurons were those that either selectively responded to checkerboard stimulus or exhibited a more significant (smaller p value) response to the checkerboard compared to the grating stimuli. In cases where p values were identical across stimulus types, we resolved ties by assigning dominance to the stimulus that explained the greater fraction of variance in the GLM. A similar definition was applied to grating-dominant neurons.

To determine whether neuronal activity was significantly modulated by facial movement independently of visually evoked responses, we quantified movement–activity coupling during inter-trial intervals (ITIs). Raw fluorescence traces were smoothed using a 5-point moving average, and stimulus-locked response epochs (defined as stimulus onset to 2.5 s post-onset) were excluded. The remaining samples were concatenated to form the ITI activity trace. Pearson correlation coefficients were computed between the z-scored ITI fluorescence trace and the simultaneously recorded, z-scored facial motion PC1 trace. To assess statistical significance while preserving the intrinsic temporal autocorrelation of the signals, we implemented a circular-shift permutation procedure. The facial motion trace was circularly shifted by a random non-zero offset relative to the neuronal trace, and the correlation was recomputed to generate a null distribution (5,000 iterations). A two-sided empirical p value was calculated as the fraction of permuted correlations whose absolute value exceeded that of the observed correlation. A neuron was classified as facial movement–related only if

it satisfied two independent criteria: (i) a significant contribution of facial movement predictors in the GLM framework (Bonferroni-adjusted $p < 0.05$), and (ii) a significant ITI correlation based on circular-shift permutation testing ($p < 0.01$).

Fitting of the functional axis based on the spatial distribution of functionally characterized neurons

To explore the relationship between spatial distribution of neurons and their functional responses, we defined a functional axis in the mediolateral (X) and anteroposterior (Y) plane, termed the X-Y functional axis, based on linear discriminant analysis (LDA). For each pairwise functional classification (e.g., checkerboard-dominant vs. grating-dominant), a linear discriminant classifier was employed to identify an axis along which the functionally distinct neurons can be maximally separated (Figure S5E). The locations of these neurons were subsequently projected onto this axis to serve as a predictor in classification models.

Quantification of projection strength and its distribution in the Laterodorsal thalamic nucleus

The projection strength in a given brain region was defined as the total length of reconstructed axon arbors within that region. To quantify this, we first registered the imaged brain to the Allen CCFv3 atlas. We then calculated the sum of the lengths of all axon centerline segments whose 3D coordinates fell within the boundaries of each target region.

To quantify the spatial distribution of axonal projections within the Laterodorsal thalamic nucleus (LD), reconstructed axon centerlines were first registered to the Allen CCFv3 atlas. For each neuron, axon traces within the LD were converted into a 3D voxelized density map. Each voxel value represented the total axon segment length contained within that voxel. Because the LD nucleus is anatomically tilted relative to the canonical coronal and horizontal planes of the Allen CCFv3 reference frame, we computed a rotation matrix that aligned the anatomical dorsal–ventral (D–V) axis of the LD with the vertical axis of the image volume. After rotation, axon density maps were projected onto the aligned D–V axis by summing voxel intensities along the orthogonal axes, yielding a one-dimensional profile representing axon length distribution as a function of D–V depth. To assess whether functional subgroups exhibited non-uniform D–V distributions, we generated null distributions by randomly shuffling neuron functional labels (3,000 permutations). For each 200 μm bin along the D–V axis, we computed the difference between observed and shuffled mean profiles. Statistical significance was evaluated using non-parametric permutation tests with Bonferroni correction across bins.

Prediction of neuronal functions based on morphological and cellular transcriptomic features

To identify structural and molecular features predictive of neuronal functional identity, we performed feature selection using stability selection combined with regularized logistic regression[38] (LassoGLM; Figure S6A). The predictor matrix included features from five categories: (1) whole-brain projection strength across brain regions, (2) soma spatial information (X-Y functional axis, dorsal-ventral axis and cortical depth), (3) axonal and dendritic morphological parameters (Figures S5C–S5E; Table S2), (4) normalized RNA-level expression of 29 genes, (5) subcellular RNA localization (subRNA-Loc) features (RNA-related features were included only in multimodal models). For subcellular RNA localization features, the high-dimensional subRNA-Loc measurements were first subjected to principal component analysis (PCA) to reduce dimensionality. The top 30 principal components (explaining 69.4% of the variance) were retained and used as predictors in the multimodal models in place of the original subRNA-Loc features. Z-score normalization was performed using only high-quality features, and features failing quality control were subsequently set to zero. For each classification task (e.g., checkerboard-dominant vs. non-responsive), binary labels were defined according to functional assignments. Stability selection was conducted by repeatedly subsampling half of the dataset across 1000 iterations. In each iteration, logistic regression was fitted using elastic net regularization ($\alpha = 0.5$). A regularization path of 100 λ values was computed without cross-validation, and model sparsity was controlled by selecting the solution whose number of non-zero coefficients (degrees of freedom) was closest to a predefined target value q. Here, q was set to $\sqrt{P}$, where P denotes the total number of candidate features, following standard stability-selection practice to limit expected false discoveries. Selection frequency for each feature was calculated as the proportion of iterations in which it was retained. Features with selection frequency ≥ 0.6 were used to train a logistic regression model for each binary classification task.[38]

Model performance was assessed using Monte Carlo 5-fold cross-validation. For each iteration, the decision threshold for binary classification was determined using Youden's index derived from training set predictions and subsequently applied to the test samples. Model performance was quantified by the area under the receiver operating characteristic curve (auROC) and classification accuracy. To evaluate statistical significance, a shuffle control was performed using 5,000 random label permutations with 5-fold cross-validation in each permutation. The mean classification accuracy from each permutation was used to generate a null distribution, against which the real model performance was compared to determine significance.

To assess the joint predictive contribution of morphological and transcriptomic information, three additional models were trained using the top 5 features ranked by stability selection frequency, drawn from (1) morphology-only, (2) transcriptome-only (RNA-level and subRNA-Loc), and (3) combined feature sets.

Estimation of the response rate of *Rbp4*$^+$ IT neurons to checkerboard stimulus

To estimate whether *Rbp4*$^+$ IT neurons exhibit a higher percentage of checkerboard-responsive cells than Thy1-GCaMP6s neurons, we assumed the observed *Rbp4*$^+$ population as a mixture of IT and PT neurons with an IT:PT ratio of 3:2.[41] Let p_total denote the observed percentage of checkerboard-responsive neurons in total *Rbp4*$^+$ population, and let p_PT be the presumed percentage of checkerboard-responsive PT neurons. For each assumed p_PT, we solved for the implied percentage of

Please cite this article in press as: Zhao et al., Multimodal imaging of gene expression, morphology, and activity of the same neuron, Cell (2026), https://doi.org/10.1016/j.cell.2026.05.041

checkerboard-responsive IT neurons (p_IT) from the mixture relation p_total = 0.6 × p_IT + 0.4 × p_PT, where 0.6 and 0.4 are mixture weights determined by the 3:2 ratio. The resulting p_IT estimates were then compared with the percentage of checkerboard-responsive neurons observed in Thy1-GCaMP6s mice using a one-sided Fisher's exact test.

2cEASI-FISH image processing and quantification

In the 2cEASI-FISH image processing pipeline (Figure S7C), raw multichannel image stacks were first split into individual fluorescence channels (405 nm, cytoDAPI; 488 nm; 546 nm and 669 nm). Cell masks were generated from cytoDAPI signals using Cellpose 3.0[75] (https://github.com/MouseLand/cellpose). mRNA puncta in the 488 nm, 546 nm, and 669 nm raw channels were detected using AIRLOCALIZE[77] (https://github.com/timotheelionnet/AIRLOCALIZE/), prior to inter-channel alignment, to minimize interpolation-related spatial error (Figure S7C; Label Images). To accurately decode dual-color encoded mRNA species, inter-channel misalignments caused by chromatic aberration and optical-mechanical shift were corrected. The 488 nm and 669 nm channels were registered to the 546 nm reference channel via affine transformation using ANTs (Advanced Normalization Tools[89]). Detected puncta coordinates in the 488 nm and 669 nm channels were then transformed using the corresponding affine matrices (Figure S7C, **Inter-channel alignment**).

Next, colocalized puncta were identified using a custom RNA-calling algorithm. Puncta within 660 nm (pre-expansion) were considered colocalized. In rare cases of dense labeling, leading to one-to-many or many-to-many colocalization, puncta were dilated into 3D spheres (660 nm radius), and their pairwise overlap volumes were used to construct a cost matrix. Optimal assignments were solved using the MATLAB "matchpair" function to maximize total overlap. Puncta present in all three channels were flagged as autofluorescence and excluded. Remaining colocalized puncta were assigned to one of six mRNA species based on dual-color coding (Figure S7C, **mRNA calling**). Manual visual inspection estimated the accuracy of mRNA calling to be ~95%.

Detected puncta were assigned to individual cells using cytoDAPI-derived segmentation masks, extracting gene identity, copy number, and 3D spatial coordinates to generate a six-gene expression matrix per round. Due to the sparse labeling of neurons, five rounds of 2cEASI-FISH were manually registered using cytoDAPI to compile a 30-gene expression profile for each neuron.

To mitigate slice-specific batch effects, gene expression level was normalized to the local reference gene *Eef2* within each tissue section. For every labeled neuron, the mean *Eef2* puncta count in a 56-μm × 56-μm × 11-μm neighborhood in the same slice was used for normalization. Normalized expression of *Gene i* in Neuron *j* was calculated as:

$G\_norm(i,j) = G\_raw(i,j) / (V\_j \times Avg\_Eef2\_Nbhd)$ where $G\_raw(i,j)$ is the raw puncta count of *Gene i* in *Neuron j*, V_j is the volume of *Neuron j*, and Avg_Eef2_Nbhd is the average *Eef2* count in the local neighborhood from the same slice in which *Neuron j* is located. The normalized values were used as the 30-gene RNA-level features for downstream analyses.

Analysis of subcellular RNA localization patterns

Decoded 3D coordinates of single mRNA molecules from 2cEASI-FISH and per-cell masks were used to quantify subcellular RNA localization (subRNA-Loc) features for each gene in each neuron. Nuclear masks were first generated from cytoDAPI image stacks with a custom nuclei model based on Cellpose-SAM,[76] followed by manual inspection and correction to ensure accurate nuclear segmentation.

To compute subRNA-Loc feature metrics, we extended the FISH-quant v2/BigFISH feature routines[48] from 2D to 3D and developed two custom modules: input_preparation3d and features3d (https://github.com/Saintgene-Xu-lab/big-fish-3D/tree/master/bigfish/classification). For each neuron and each gene, the functions take as input (i) a 3D cell mask, (ii) a 3D nuclear mask, and (iii) the 3D mRNA coordinates, and return the full set of BigFISH subcellular-localization features in 3D.

We chose eight interpretable features motivated by prior literature,[48,49] as summarized below.

Polarization Index (PI) quantifies the axial polarization of RNA puncta; Dispersion Index (DI) reflects the spatial spread of RNA molecules; Peripheral Distribution Index (PDI) measures nuclear-peripheral bias; Cell Edge Index (CEI) reports RNA enrichment adjacent to the cell boundary (within 500 nm); Nuclear Edge Index (NEI) reports RNA enrichment near the nuclear boundary (within 500 nm); Mean Nuclear Distance Index (MNDI) calculates mean distance of RNAs to the nuclear boundary normalized by the mean distance of all intracellular voxels to the nuclear boundary; Mean Cell Distance Index (MCDI) computes mean distance of RNAs to the cell boundary normalized by the mean boundary distance of all intracellular voxels; and Intranuclear Index (INI) is defined as the ratio of proportion_rna_in_nuc to proportion_nuc_volume and represents intranuclear enrichment of RNA puncta.

For each neuron, per-gene values of these 8 features yielded a 240-dimensional subRNA-Loc vector (30 genes × 8 features) used for downstream analyses.

Unsupervised clustering of neurons based on RNA-level and subRNA-Loc features

Unsupervised clustering was performed separately for RNA-level and subRNA-Loc features using Seurat *v5.3.0*.[90] For both analyses, data were converted into Seurat objects using the "*CreateSeuratObject*" function. RNA-level data (excluding *Eef2*) were normalized using the "*NormalizeData*" function and scaled using "*ScaleData*", while subRNA-Loc features were directly scaled using "*ScaleData*". Principal component analysis (PCA) was applied to identify dominant patterns of variation, with the top components selected for downstream analyses. Cell clustering was conducted using the "*FindNeighbors*" and "*FindClusters*" functions, and two-dimensional visualization was achieved through UMAP dimensionality reduction using "*RunUMAP*" and visualization with "*DimPlot*". For the 141 excitatory neurons (Figures 5E-5G), RNA-level analysis used the top 6 principal components for "*FindNeighbors*" (dims = 1:6,

Please cite this article in press as: Zhao et al., Multimodal imaging of gene expression, morphology, and activity of the same neuron, Cell (2026), https://doi.org/10.1016/j.cell.2026.05.041

k.param = 18) and "*FindClusters*" (resolution = 0.31, algorithm=1), with UMAP visualization parameters (dims = 1:6, n.neighbors = 20). The corresponding SubRNA-Loc analysis (Figures 5K and 5L) utilized the top 3 principal components for "*FindNeighbors*" (dims = 1:3, k.param = 25) and "*FindClusters*" (resolution = 0.56, algorithm = 4), with UMAP parameters (dims = 1:4, n.neighbors = 25, spread = 0.9). For the 105 PT neurons (Figures 6A and 6B), RNA-level analysis employed "*FindNeighbors*" (dims = 1:5, k.param = 19), "*FindClusters*" (resolution = 0.53, algorithm = 1), and UMAP (dims = 1:15, n.neighbors = 30), while SubRNA-Loc analysis used "*FindNeighbors*" (dims = 1:5, k.param = 21), "*FindClusters*" (resolution = 1.95, algorithm = 4), and UMAP (dims = 1:5, n.neighbors = 30, spread = 0.5). Top marker genes for each cluster identified by "*FindAllMarkers*" were visualized using ComplexHeatmap, and final Seurat clusters were aligned with multimodal neuron labels to generate Sankey plots.

Axon-length and gene-expression variability analysis

To compare intra-class variability between IT and PT neurons, we used total axon length as a quantitative proxy for axonal morphological diversity and computed pairwise distances in axon length and gene expression within each projection class. Axon-length distance matrices were calculated as absolute differences between normalized axon lengths (*z*-scored across the dataset). Gene-expression variability was quantified as pairwise Euclidean distances computed on either normalized 29-gene expression vectors or normalized *Rorb* expression alone (both *z*-scored across the dataset). Distributions of within-class pairwise distances were compared between IT and PT neurons using two-sided Wilcoxon rank-sum tests (Figures S8B, S8C, and S8E).

To examine the relationship between structural and molecular variability within IT neurons, we assessed the correlation between the axon-length distance matrix and the corresponding gene-expression distance matrices (29-gene or *Rorb*) using a Mantel test (Spearman's r, 10,000 permutations) to account for non-independence among pairwise distances. Empirical *p* values were obtained by randomly permuting neuron identities in the distance matrices. For visualization (Figures S8D and S8F), IT neuron pairs were grouped into five quantiles based on axon-length distances, and the corresponding gene-expression distances were displayed as violin plots overlaid with a linear regression fit and 95% confidence bands.

Subtyping and classification of checkerboard-responsive PT neurons

We selected neurons classified as PT and checkerboard-responsive based on GLM-derived functional subtyping (n = 28) and performed unsupervised hierarchical clustering using normalized *Vip* expression and 3D soma coordinates (medial-lateral [M-L], dorsal-ventral [D-V], anterior-posterior [A-P], and cortical depth). Pairwise correlation distances were computed among these neurons, followed by agglomerative clustering with average linkage to partition the dendrogram into two principal subtypes (C1 and C2; Figure 6K).

Stimulus-aligned response dynamics were quantified using t-auROC (using the 1.8 to 0.2 s period prior to stimulus onset as a baseline, and a 0.33 s moving window) as previously described.[4] We employed this metric rather than average calcium responses because it comprehensively accounts for both the average response magnitude and trial-to-trial consistency. Significant temporal divergence between C1 and C2 was defined by a two-sided unpaired t-test ($p < 0.05$) sustained for > 200 ms (Figure 6L). Overall response magnitudes (area under the t-auROC curve after stimulus onset), *Vip* expression, and soma coordinates were compared between the subtypes using two-sided Wilcoxon rank-sum tests with Benjamini-Hochberg (BH) false discovery rate (FDR) correction (Figures 6N and 6O).

To evaluate the discriminative capacity of the identified features, we trained an L2-regularized logistic regression classifier to distinguish C2 from C1 using solely *Vip* expression and M-L position. Classifier performance was evaluated via Monte Carlo 5-fold cross-validation, following the procedures detailed in the section "Prediction of functions based on morphological and cellular transcriptomic features" (Figures 6P and 6Q).

ASSESSMENT OF RNA PRESERVATION FOLLOWING CLEARING AND REHYDRATION

Following RNase-free perfusion as mentioned above, mouse brains were bisected along the midsagittal plane. One hemisphere underwent tissue clearing, rehydration, structural imaging, and was then sectioned at 200 μm thickness (treated). The contralateral hemisphere was directly sectioned at the same thickness and preserved in 70% ethanol (untreated). Adjacent sections from VISp of both treated and untreated samples were embedded in hydrogel and subjected to two rounds of EASI-FISH targeting six representative genes using the previously established EASI-FISH protocol (Figure S7C). Round 1 included *Vglut1* (excitatory neuron marker), *Gad1* (inhibitory neuron marker), and *Eef2* (housekeeping reference). Round 2 targeted *Rprm* (layer 4/5-enriched), *Npy* (highly expressed neuropeptide), and *Satb2* (moderately expressed cortical marker). To evaluate RNA preservation, four regions of interest (ROIs, 327.61 μm × 321.99 μm post-expansion) spanning the dorsoventral axis were imaged per sample using a 20× objective (zoom 1.0×). Gene expression profiles of individual neurons were extracted using standard EASI-FISH analysis pipeline, with Cellpose[91] replacing Starfinity[92,93] for cell segmentation. Gene expression patterns were visualized and compared between treated and untreated groups (Figures S7C and S7D). Additionally, the fraction of neurons positively expressing each gene (defined as count > 0) was measured and compared between the two conditions (Figure S7E).

Rbp4 expression in Rbp4-Cre::GCaMP6s, Thy1-GCaMP6s and Rbp4-Cre VISp neurons

Rbp4-Cre mice injected with AAV-hSyn-FLEX-GCaMP6s in the VISp (See Mice preparation; Rbp4-Cre::GCaMP6s), Thy1-GCaMP6s, and Rbp4-Cre mice were perfused under RNase-free conditions as previously described. Brains were coronally sectioned into

Please cite this article in press as: Zhao et al., Multimodal imaging of gene expression, morphology, and activity of the same neuron, Cell (2026), https://doi.org/10.1016/j.cell.2026.05.041

200-μm coronal slices and stored in 70% ethanol. EASI-FISH was employed to quantify *Rbp4* mRNA expression across these lines. In Thy1-GCaMP6s sections, GCaMP6s fluorescence was quenched after EASI-FISH treatment; therefore, *mEGFP* and *Rbp4* mRNAs were co-detected to identify labeled neurons and assess *Rbp4* expression. In contrast, GCaMP6s fluorescence was preserved in Rbp4-Cre::GCaMP6s sections, enabling direct localization of labeled neurons; only *Rbp4* mRNA was probed. To further verify *Rbp4* expression specificity in Rbp4-Cre mice, *Rbp4*, *Vglut1*, and *Cre* mRNAs were simultaneously detected in Rbp4-Cre sections. Cells were classified as Cre^{+} (> 5 puncta) and $Vglut1^{+}$ (> 10 puncta). Image processing and quantification were performed as described in the section "2cEASI-FISH image processing and quantification".

Analysis of scRNA-seq data from the ABC Atlas

To verify gene expression profiles in our 2cEASI-FISH dataset, we analyzed publicly available scRNA-seq data from the mouse visual cortex (VIS), obtained from the ABC Atlas[51] (WMB-10Xv3-Isocortex-1; https://alleninstitute.github.io/abc_atlas_access/descriptions/WMB-10Xv3.html). Raw gene expression matrices generated by 10× Genomics were imported into *Scanpy*[94] (V1.11.1, https://github.com/scverse/scanpy) for processing. Expression values were normalized using "*sc.pp.normalize_total*" (target sum = 1e4, equivalent to counts per million), followed by log-transformation using "*sc.pp.log1p*". Cells were retained if they expressed at least one gene from a predefined target panel, with expression values greater than 0 considered gene-positive. The selected panels included *Vglut1*, *Gad1*, and *Vip* (Figure S8A, left); *Vglut1*, *Gad1*, and *Pvalb* (Figure S8A, right); and *Rbp4*, *Vglut1*, and *Gad1* (Figure S8J). All downstream analyses were restricted to this filtered subset of cells and genes. Visualizations were generated using custom Python scripts (V3.13.2).

To further validate *Rbp4* expression in the Rbp4-Cre line, we analyzed SMART-seq scRNA-seq data from Cre-driver lines in the mouse VISp obtained from the Allen Brain Atlas (GSE115746), including the Rbp4-Cre and Vglut1-Cre datasets. The two datasets were integrated using Seurat with the "*FindIntegrationAnchors*" (anchor.features=2500, reduction="cca") and "*IntegrateData*" (dims = 1:30) functions. The integrated object was subsetted to retain excitatory neurons (*Slc17a7* > 1) and further filtered to include only *Rbp4*-expressing cells (*Rbp4* > 0). Log-normalized *Rbp4* expression levels in both genotypes were visualized using violin plots ("VlnPlot") and compared using the two-sided Wilcoxon rank-sum test. If Cre labeling mirrored endogenous *Rbp4* transcription in a strictly binary manner, then the *Rbp4* expression distributions among these *Rbp4*-expressing excitatory neurons (*Rbp4* > 0) should be comparable between these two mouse lines. Instead, Rbp4-Cre neurons exhibited significantly higher *Rbp4* expression than Vglut1-Cre neurons (Figure S8H). This supports a continuum enrichment model by the Rbp4-Cre driver, indicating that non-targeted (Cre^{-}) excitatory neurons can still carry low-level Rbp4 transcripts.